

# Optical Engineering

OpticalEngineering.SPIEDigitalLibrary.org

## **Review of terahertz photoconductive antenna technology**

Nathan M. Burford  
Magda O. El-Shenawee

# Review of terahertz photoconductive antenna technology

Nathan M. Burford<sup>a,\*</sup> and Magda O. El-Shenawee<sup>b</sup>

<sup>a</sup>University of Arkansas, Microelectronics-Photonics Program, 731 West Dickson Street, Fayetteville, Arkansas 72701, United States

<sup>b</sup>University of Arkansas, Department of Electrical Engineering, 3217 Bell Engineering Center, Fayetteville, Arkansas 72701, United States

**Abstract.** Photoconductive antennas (PCAs) have been extensively utilized for the generation and detection of both pulsed broadband and single frequency continuous wave terahertz (THz) band radiation. These devices form the basis of many THz imaging and spectroscopy systems, which have demonstrated promising applications in various industries and research fields. The development of THz PCA technology through the last 30 years is reviewed. The key modalities of improving device performance are identified, and literature is reviewed to summarize the progress made in these areas. The goal of this review is to provide a collection of all relevant literature to bring researchers up to date on the current state and remaining challenges of THz PCA technology. © 2017 Society of Photo-Optical Instrumentation Engineers (SPIE) [DOI: 10.1117/1.OE.56.1.010901]

Keywords: terahertz; photoconductive antenna; spectroscopy.

Paper 161629V received Oct. 19, 2016; accepted for publication Dec. 29, 2016; published online Jan. 24, 2017.

## 1 Introduction to Terahertz Photoconductive Antennas

Terahertz (THz) is the name given to the region of the electromagnetic spectrum lying between the microwave band (<100 GHz) and the far infrared band (>10 THz).<sup>1</sup> This region is often referred to as “the last frontier” for electromagnetic waves, since historically there has been comparatively little work observing the science and develop the applications of THz waves. The reason for this is simple; efficient generation and detection of THz is an exceedingly nontrivial problem. THz lies in the transitional region of the electromagnetic spectrum between the classically described electronics region (radio, microwaves and millimeter waves) and the photonic region (infrared, visible, UV, and x-ray), where the quantum nature of light becomes dominant. Approaching the THz regime from either of these regions comes with unique challenges. Increasing the operating frequency of microwave devices is limited by the carrier mobility of the oscillating semiconductor.<sup>2</sup> On the other hand, reducing the energy of emitted photons generated by electron transitions in a semiconductor is inhibited by the fact that the energy of THz photons is less than the thermal energy at room temperature.<sup>3</sup> Other methods, that combine aspects of both photonics and electronics<sup>4,5</sup> have been utilized, though these come with their own list of challenges.

However, the challenges facing the various methods of THz generation and detection have not stopped the development of this technology. Although THz technology is not nearly as mature as that of other regions of the electromagnetic spectrum, many practical applications have been proposed and are currently under development. One of the earliest commercial applications of THz imaging and spectroscopy is nondestructive screening of pharmaceuticals. Changes in solid state crystal form<sup>6</sup> and spectral fingerprinting of chemical compounds have been demonstrated.<sup>7,8</sup> Spectral fingerprinting has been proposed for security applications as well, since the nondestructive nature of THz waves

could allow penetration into materials to detect hidden narcotics and explosives.<sup>9–11</sup> Many works have studied the potential use of THz imaging and time-domain reflectometry as a quality control tool in electronics fabrication and packaging<sup>12–20</sup> as well as composite material inspection.<sup>21</sup> Biomedical imaging using THz radiation has been proposed and studied for the purpose of cancer imaging,<sup>22–28</sup> burn wound assessment,<sup>29–32</sup> and dental tissue imaging.<sup>33</sup> Many other applications exist as well, and several in-depth reviews are available for the various applications of THz imaging and spectroscopy technology.<sup>9,10,24,34–41</sup>

This review will focus mostly on the various key aspects of THz photoconductive antenna (PCA) technology, while selected other technologies, such as photomixers, unbiased surface emission, and optical rectification, will be discussed briefly. The fundamental theories of THz generation in PCAs will be discussed in detail. Key works from the literature will be categorically reviewed and organized as follows: photoconductive material development, large area emitters, plasmonic nanostructures, broadband performance improvement, and commercially available systems.

### 1.1 Theory of Terahertz Photoconductive Antennas

Emission and detection of pulsed broadband THz radiation from optically pumped PCAs was first accomplished in the late 1980s by the research groups of THz pioneers David Auston<sup>42–45</sup> and Daniel Grischkowsky.<sup>1,46,47</sup> The concept of generation of pulsed THz radiation from a PCA is illustrated in Fig. 1(a). Here, an example of a femtosecond optical pulse with a pulse duration of <1 ps is incident on a PCA. The PCA consists of a DC biased metal dipole antenna patterned on a photoconductive substrate. The optical pulse is incident on the antenna gap (G), propagates into the photoconductor, and begins to generate photocarriers inside the photoconductor as it is absorbed, as shown in Fig. 1. The generated photocarriers are accelerated in the DC bias field, producing a transient photocurrent, which drives the dipole antenna and ultimately re-emits as a THz frequency pulse.<sup>42–45,48,49</sup> The transient response of the PCA is illustrated in Figs. 1(b)–1(e). As the optical pulse is absorbed

\*Address all correspondence to: Nathan M. Burford, E-mail: [nburford@uark.edu](mailto:nburford@uark.edu)

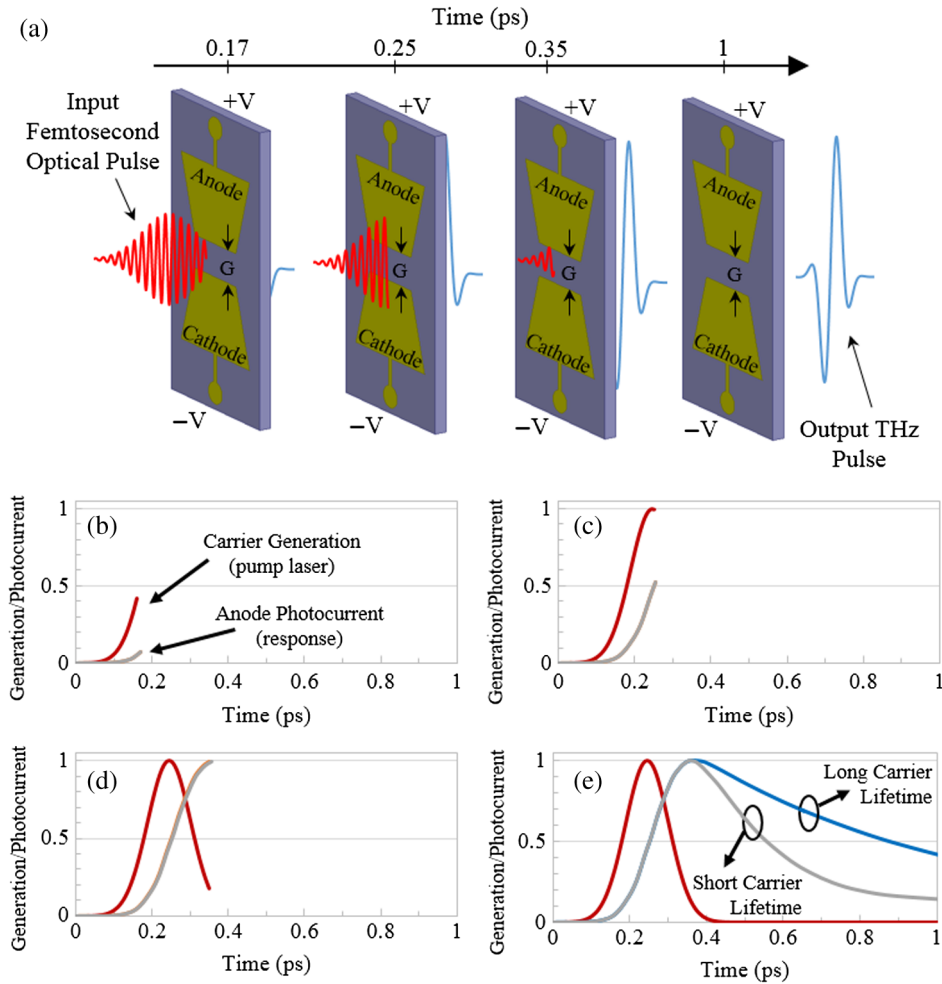


**Fig. 1** Illustrative example of pulsed THz generation in a PCA. (a) Femtosecond optical pulse propagates into the photoconductor, generates a transient photocurrent, which drives the antenna, and is re-emitted as a broadband THz pulse. (b–e) Time profile of the carrier generation (red trace) and photocurrent in the antenna gap for photoconductive material (gray trace) for short-carrier lifetime and (blue trace) for long carrier lifetime.

in the photoconductor, carriers are generated at a rate proportional to the optical pulse (red trace). The photocarriers respond by accelerating along the DC bias field, thus generating a transient photocurrent with a rise time approximately proportional to the incident optical pulse rise time (gray trace). After the photocurrent peaks, as shown in Fig. 1(d), the decay time is then dictated by the electrical properties of the photoconductor rather than the temporal profile of the optical pulse.<sup>48</sup> As shown in Fig. 1(e), if the photoconductor has a short carrier lifetime (gray trace), the photocarriers generated by the optical pulse will begin to recombine immediately after the optical pulse is fully absorbed.<sup>48–50</sup> By contrast, if the photoconductor has a long carrier lifetime (blue trace), the generated photocarriers will continue to contribute to the photocurrent after the optical pulse is fully absorbed. This has the effect of broadening the photocurrent pulse, which would in turn broaden the output pulse and reduce the overall THz frequency bandwidth. To prevent this, photoconductors with subpicosecond carrier lifetime are often utilized, with low temperature grown gallium arsenide (LT-GaAs) being the most common.<sup>51–64</sup>

An approximately to-scale illustration of a typical THz PCA is shown in Fig. 2. The isometric view in Fig. 2(a)

illustrates the main device components, which include the photoconductive substrate, THz dipole antenna electrodes, and high-resistivity float-zone silicon (HRFZ Si) lens. THz waves are generated at the antenna dipole, where the optical pump is focused. The THz radiation propagates along the axis of the optical pump, into the photoconductive substrate and then into air, with the majority propagating into the substrate.<sup>65</sup> The HRFZ Si lens couples with the generated THz radiation and propagates it into free space. Top views of the full area and enlarged dipole regions are shown in Figs. 2(b) and 2(c), respectively. Here, it can be seen that parallel microstrip lines connect the centrally located dipole antenna to larger bias pads. These bias pads act as a large electrical surface connection for wire bonding to external circuitry that is used to apply the DC bias voltage. The overall lateral dimension  $L$  of the device is typically in the range of a few millimeters to around a centimeter. The antenna dipole length  $D$  is typically on the order of 100  $\mu\text{m}$ , while the gap dimension  $G$  can range from a few micrometers to almost  $D$ .

Detection of the emitted THz pulses is often accomplished either through the use of calibrated THz power detectors, such as bolometers<sup>34,55,66–69</sup> and pyroelectric

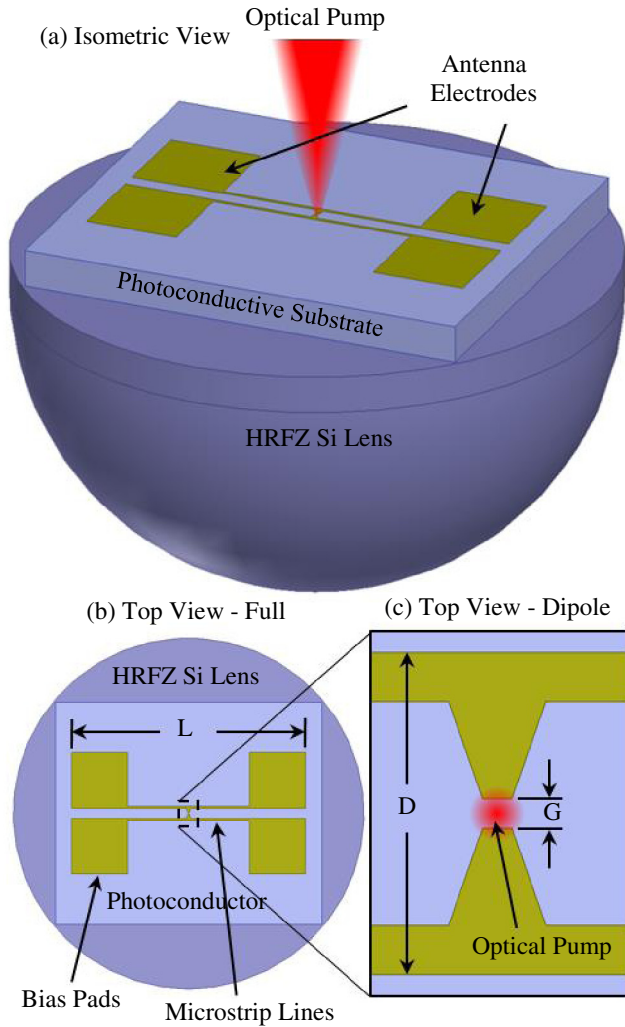


**Fig. 2** (a) Isometric view of a typical THz PCA device mounted on a HRFZ Si lens. (b) Full top view of the THz PCA and (c) expanded top view of the centrally located THz dipole structure only showing gap dimension  $G$  and dipole length  $D$ .

detectors,<sup>10,70–74</sup> or more completely by electro-optic sampling of the THz pulse in a time-domain spectroscopy (TDS) configuration.<sup>8,43,44,48,72,75</sup> The later method allows extraction of the temporal profile of the THz field. The schematic of a THz time-domain system is shown in Fig. 3. THz is generated through the previously described conversion of a femtosecond optical pulse to broadband THz pulse at the emitter.<sup>42–45,48,49</sup> The emitter is biased with a DC voltage, and often the time-averaged photocurrent is measured as well. In general, the power of the emitted THz pulse is proportional to the measured photocurrent across the dipole antenna.<sup>48,50,76,77</sup>

To measure the emitted THz pulse, another PCA is utilized as the receiver. Unlike the emitter, the receiver PCA does not have an external DC bias. Instead, the emitted THz beam is focused on the dipole antenna, so the beam polarization is aligned across the antenna gap.<sup>1,48,78</sup> As the THz pulse propagates into the antenna, it induces a transient bias voltage across the gap. To measure this transient voltage, a portion of the femtosecond optical pulse is split from the source beam, propagates through an adjustable optical delay line, and focuses in the gap of the receiver PCA.

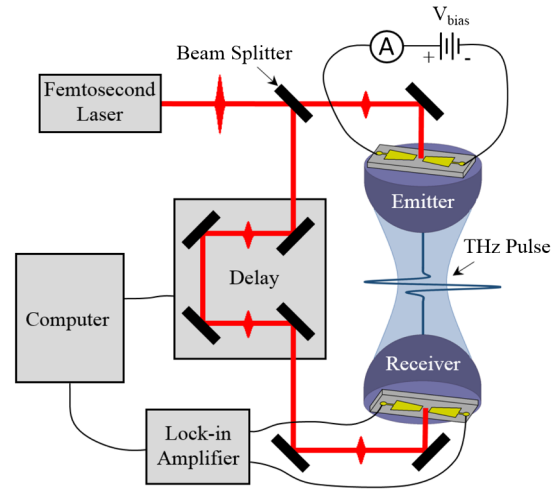


**Fig. 3** Schematic diagram of the typical configuration of electro-optic sampling of THz pulses in a TDS system.

This provides a narrow impulse of photocarriers at a time that can be controlled by the optical delay line. When the photocarrier impulse and THz field induces transient voltage overlap in time, a measurable photocurrent proportional to the instantaneous antenna voltage is induced across the antenna. By sweeping the optical delay line, the photocarrier impulse signal is convoluted with the THz field induced transient voltage signal. Collecting and correlating both the optical delay position and induced photocurrent data allows the temporal profile of the THz pulse to be measured. The coherent nature of this detection method provides a high signal-to-noise ratio (SNR), since it greatly reduces the effects of blackbody radiation and other sources of THz radiation on the receiver.<sup>78</sup>

Although the exact nature of THz generation in PCAs is not universally agreed upon, currently, there are three main modalities in which THz generation in a PCA can be explained: the transient acceleration of carriers in the bulk semiconductor,<sup>56,67,77,79</sup> the instantaneous drop in dipole gap resistivity after optical pulse absorption,<sup>50,80</sup> and the direct collection of photocarriers by the antenna electrodes.<sup>72,76,81,82</sup> When a femtosecond optical pulse is incident in the gap of a THz PCA, electron–hole pairs are generated everywhere in the gap, proportional to the local intensity of the incident optical pulse.<sup>48,50,77</sup> The photocarriers are accelerated along the DC bias field and recombined a short distance later. This induces time-varying surface currents on the device structure, which in turn produces a propagating THz pulse with the electric field  $E_{\text{THz}}$  described by Ref. 77:

$$E_{\text{THz}}(r, t) = -\frac{1}{4\pi\epsilon_0 c^2} \frac{\partial}{\partial t} \int \frac{J_s(r', t - \frac{|r-r'|}{c})}{|r-r'|} ds', \quad (1)$$

where  $J_s$  is the spatially and temporally dependent surface current on the emitter surface,  $r$  is the spatial vector of the location of the THz field,  $r'$  is spatial vector of the location of the surface current, which is integrated across the emitter surface  $ds'$ ,  $c$  is the speed of light in vacuum, and  $\epsilon_0$  is the permittivity of free space. From Eq. (1), it can be seen that the radiated THz field will be dependent on the net surface currents in a PCA emitter. By considering

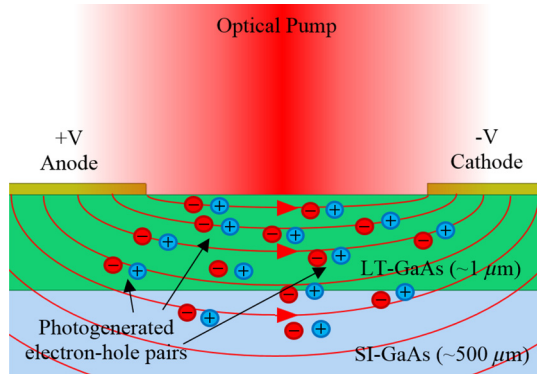


**Fig. 4** Cross-section illustration of optical carrier generation at the dipole gap of a LT-GaAs based THz PCA showing the flux lines of the electric field in red arrows.

the various sources of surface currents, it is possible to describe the different mechanisms of THz emission.<sup>48,50,77</sup>

To understand the various mechanisms that produce THz radiation in a PCA, consider the cross-section illustration of a THz PCA dipole shown in Fig. 4. A typical device architecture, which includes metal anode and cathode on a  $\sim 1\text{-}\mu\text{m}$  thick LT-GaAs photoconducting layer above a  $\sim 500\text{-}\mu\text{m}$  thick semi-insulating GaAs (SI-GaAs) substrate, is shown. The first cause of THz generation arises directly from the generation and acceleration of charge in the photoconductor known as the current surge model.<sup>73</sup> Electron-hole pairs generated in the gap will be separated; they accelerate along the bias electric field, as shown in Fig. 4, and recombine a short time later.<sup>56,73,79,83</sup> For the second cause of THz generation, consider the state of the PCA device prior to optical excitation. Due to the parallel-line nature of the device, there is a capacitive energy stored across the gap in the form of positive and negative charge accumulation at the anode and cathode, respectively.<sup>80</sup> The magnitude of this charge is dependent on the device geometry, bias voltage, and gap resistivity.<sup>80,84</sup> The gap resistivity, which also determines the bias electric field distribution in the photoconductor, is dependent on the carrier concentration inside the photoconductor. Exciting the gap with an optical pulse causes a sharp rise in the carrier concentration and, consequently, a drop in resistivity. This causes a THz frequency oscillation in the antenna metallization as the bias field responds.<sup>48,77,80</sup> The third cause of THz generation comes from optical injection of current directly into the antenna electrodes.<sup>77,80,85</sup> Any photocarriers generated in sufficient proximity to the antenna electrodes will be collected by the antenna before they recombine. This acts as a driving current that, provided the induced current pulse is sufficiently short, also induces THz oscillations in the antenna.<sup>77,80,85</sup>

Often, the performance of THz PCA-based systems is described by one or more of the following metrics: system SNR, strength of the THz signal, bandwidth of the THz signal, and optical-to-THz conversion efficiency.<sup>36</sup> The SNR of a THz PCA system depends on several complex factors besides the THz PCA emitter.<sup>86,87</sup> SNR is often defined as the ratio of the peak signal in the frequency-domain spectra with the amplitude of the system noise (i.e., the measured RMS signal amplitude at the detector when the THz beam is blocked). The strength of the THz signal depends on the THz PCA emitter material and configuration, as well as the

applied bias voltage and incident optical pump power. Generally, the signal strength is expressed as the time-average of the output THz power or the peak in the output THz electric field. With the more recent advent of higher-power THz emitters, the optical-to-THz conversion efficiency has arisen as an additional performance metric.<sup>76</sup> This is a useful metric to compare the total input optical power to the total output THz power.

Increasing the signal strength in a THz PCA-based system would be useful for applications where signal penetration into lossy materials is necessary, including biomedical imaging,<sup>25,26,30</sup> biological applications such as mapping water content in leaves,<sup>88,89</sup> security screening,<sup>9-11</sup> and others. Similar to the SNR metric, the bandwidth depends on several factors in a THz system other than the PCA emitter. Unlike radio frequency antennas, where the frequency bandwidth is determined by the  $-10$  dB range, the THz bandwidth of a PCA is often expressed as the range of frequencies, where the measured frequency-domain signal strength exceeds the system noise level. Increased bandwidth is important for applications that utilize distinct spectral characteristics in materials.<sup>7,8</sup> For example, THz imaging and spectroscopy for pharmaceuticals requires the ability to observe narrow absorption peaks in the THz band. Therefore, increasing the bandwidth of a THz PCA-based system could allow additional vibrational modes to be quantified.<sup>7,8</sup>

## 2 Photoconductive Material Development

### 2.1 Challenges

Since the first demonstrations of early photoconductive switches, the main factor enabling their effective performance has been the selection of specific photoconductive materials with necessary electro-optic characteristics.<sup>43,51,52,90</sup> The common perception is that for a PCA emitter or detector to have broadband performance, the photoconductive material must have a subpicosecond carrier lifetime. However, carrier lifetime is only one of several material properties dictating a PCA's overall performance for a particular application. In addition to a low carrier lifetime, maintenance of relatively high carrier mobility, appropriate bandgap, high breakdown voltage, suppression of zero bias photocurrent, and maximizing the material dark resistivity play a role in a complex relationship, which influences a PCA's output power, maximum optical pump power and bias voltage, bandwidth, and SNR.<sup>57,80,86,91,92</sup>

Thus far, the most studied and promising materials for THz PCAs have included bulk gallium arsenide (GaAs),<sup>51-64</sup> bulk indium gallium arsenide (InGaAs),<sup>69,87,93-99</sup> alternating nanoscale multilayers of InGaAs and indium aluminum arsenide (InAlAs),<sup>100-107</sup> and select other group III-VI semiconductors.<sup>91,108-111</sup> The following sections will individually address each material system, reviewing key works and summarizing their unique contributions and applications to the development of THz PCA technology.

### 2.2 Gallium Arsenide

Although the earliest demonstrations of PCA technology utilized argon ion ( $\text{Ar}^{3+}$ ) irradiated crystalline silicon epitaxially grown on sapphire (SOS),<sup>43,90</sup> GaAs has long been the preferred material for PCAs. GaAs has a room temperature bandgap of 1.424 eV (871 nm),<sup>112</sup> making it compatible with

the titanium-doped sapphire ( $\text{Ti}^{3+}$ :sapphire) femtosecond-pulsed laser sources commonly used to excite PCAs. GaAs is normally utilized in one of three forms: SI-GaAs, LT-GaAs, and ion-implanted GaAs, such as nitrogen ( $\text{GaAs:N}^{3-}$ ).

Early works by Warren et al.,<sup>51</sup> Gupta et al.,<sup>52</sup> and Harmon et al.<sup>53</sup> studied the effects of GaAs growth temperature on the carrier lifetime and THz PCA performance. Warren et al.<sup>51</sup> utilized LT-GaAs (250°C growth temperature), SI-GaAs and SOS based PCAs in a THz TDS setup to compare the effectiveness of each as both transmitters and receivers. Under 70-fs optical pulse excitation, identical performance was found in the SI-GaAs and LT-GaAs samples acting as emitters, with both the LT-GaAs and SOS acting as receivers. This indicated similar quality in the crystal structure of the GaAs samples. Comparing the configuration using GaAs samples as both emitter and receiver with the configuration using only SOS samples demonstrated five times higher peak in the detected THz signal and a 0.71-ps pulse width.<sup>51</sup> Gupta et al.<sup>52</sup> compared PCA performance in a TDS configuration using LT-GaAs and chromium-doped GaAs ( $\text{GaAs:Cr}^{3+}$ ). For the LT-GaAs samples, the LT-GaAs was grown by molecular beam epitaxy (MBE) at temperatures between 200°C and 250°C. GaAs growth in this temperature range leads to two benefits: high level of crystallinity, which in turn leads to higher carrier mobility, and excess  $\text{As}^{3+}$  within the crystal structure manifesting as point defects. These point defects act as recombination centers, drastically reducing the carrier lifetime. Gupta et al.<sup>52</sup> showed that LT-GaAs samples grown at 190°C and 200°C yielded a carrier lifetime below 400 fs. By comparison, the  $\text{GaAs:Cr}^{3+}$  samples grown at temperatures above 250°C yielded carrier lifetimes greater than 50 ps.<sup>52</sup> The work of Harmon et al.<sup>53</sup> further explained the nature of growth temperature and postgrowth annealing on GaAs carrier lifetime. Here, GaAs thin films were epitaxially grown on top of sacrificially lift-off layer to allow removal and differential transmission measurements to be performed. Differential transmission measurements allowed the carrier lifetime to be derived. By combining this with transmission electron microscope (TEM) imaging, it was found that the carrier lifetime is directly related to the spacing of the excess  $\text{As}^{3+}$  clusters.<sup>53</sup> Spacing and diameter of the arsenic clusters as a function of anneal temperature was extracted from the TEM data for films with two different growth temperatures, 250°C and 320°C, as shown in Fig. 5 (Fig. 1 in Ref. 53).<sup>53</sup>

Tani et al.<sup>54</sup> studied LT-GaAs growth temperature and anneal time effects along with their performance characteristics when implemented in THz PCA emitters.<sup>55</sup> LT-GaAs grown at 250°C and annealed postgrowth at 600°C for 5 min was found to yield a 0.3-ps carrier lifetime.<sup>54</sup> PCA dipoles with different electrode shapes were fabricated and compared with SI-GaAs with a ~100-ps carrier lifetime.<sup>55</sup> As with the results of Gupta et al.,<sup>52</sup> the emitted pulse shapes of both emitters were comparable, with the amplitude of the SI-GaAs based emitter being over five times higher than the LT-GaAs emitter.<sup>55</sup> However, this was observed at relatively low optical pump power (15 mW) and low DC bias (30 V). Analysis of the dark I-V and output THz power versus input optical power characteristics showed the LT-GaAs based emitters to have higher saturation thresholds as compared to the SI-GaAs. At biases above 5 V, the LT-GaAs emitter showed a linear  $I - V$  relationship for bias

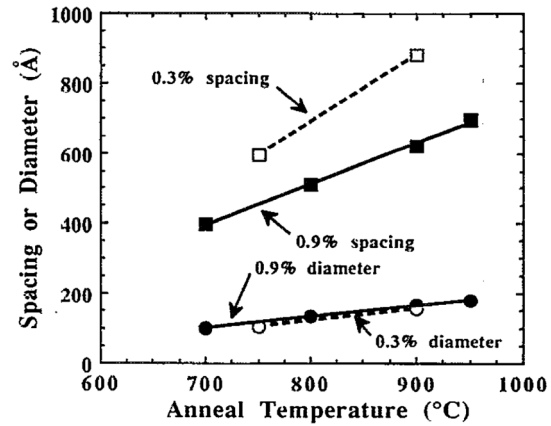
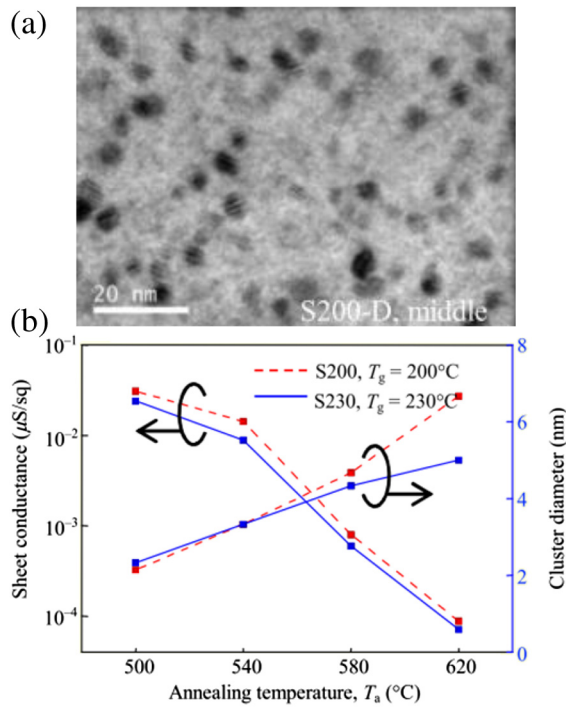


Fig. 5 Precipitate diameter and precipitate spacing versus 30-s anneal for the two LT-GaAs films used in this study.<sup>53</sup> Reprinted from Ref. 53, with permission of AIP Publishing.

fields as high as 200 kV/cm, with a drastically higher dark resistance compared to the SI-GaAs emitter. Higher dark resistance indicated a higher breakdown voltage and was demonstrated by showing breakdown in a 5  $\mu\text{m}$  gap dipole at biases of 160 V for the LT-GaAs, as compared with 50 to 70 V for the SI-GaAs.<sup>55</sup> Similar work by Stone et al.<sup>56</sup> compared SI and LT-GaAs PCAs with various large electrode dipole geometries. Triangular, circular, and square dipoles were characterized using a Golay cell detector to measure their power emission spectrum, with the frequency-domain peak frequency location and FWHM bandwidth being the comparing factors.<sup>56</sup> In all geometries, the LT-GaAs based emitters had higher peak frequency and higher bandwidth, with the largest bandwidth of 0.9 THz being observed in the LT-GaAs based circular dipole.<sup>56</sup> Additionally, it was observed that for conditions yielding similar output THz power, the LT-GaAs based emitters produced lower photocurrent than their SI-GaAs based counterparts.<sup>56</sup> With lower photocurrent, thermal effects arising from high optical pump power and bias voltages were reduced.<sup>56</sup> Later work by Moon et al.<sup>57</sup> demonstrated that postgrowth annealing of LT-GaAs allowed the sheet resistance and carrier lifetime to be manipulated. Annealing causes the excess  $\text{As}^{3+}$  precipitates to form clusters within the crystal structure, the size and spacing of which are controlled by growth temperature and postgrowth anneal temperature. Removing the  $\text{As}^{3+}$  precipitates from their uniform distribution as antisites in the crystal structure had the positive effect of increasing the material resistance, as well as the negative effect of increasing the carrier lifetime.<sup>57</sup> TEM imaging of the postgrowth annealed LT-GaAs as well as the relationship between sheet conductance and cluster diameter with anneal temperature is shown in Fig. 6 [Figs. 2(a) and 3(a) in Ref. 57].<sup>57</sup> It was shown that for a given growth temperature, the postgrown anneal temperature can be tuned to yield an optimum THz emission performance. It was found that in the range of 500°C to 620°C, the maximum peak-to-peak THz pulse intensity was observed for postgrowth anneal temperatures between 540°C and 580°C, for growth temperatures of 200°C and 230°C.<sup>57</sup>

In addition to low-temperature growth, several groups have investigated the use of ion-implanted GaAs for THz.<sup>58-64</sup> Liu et al.<sup>58,59</sup> characterized the effect of  $\text{As}^{3+}$



**Fig. 6** (a) TEM photograph of annealed LT-GaAs layer and (b) sheet conductance and cluster diameter as functions of annealing temperature. Reproduced from Ref. 57 with permission from the Electronics and Telecommunications Research Institute.

ion implantation of SI-GaAs acting as both PCA emitters and receivers. Similar to low-temperature growth of GaAs, ion implantation of  $\text{As}^{3+}$  in SI-GaAs introduces excess  $\text{As}^{3+}$  impurities within the crystal structure. However, GaAs:As $^{3+}$  was claimed to have a benefit of improved controllability of the excess  $\text{As}^{3+}$  concentration and uniformity as compared to LT-GaAs. Although performance of the two materials is comparable at low bias voltage, the GaAs:As $^{3+}$  PCA exhibited a higher bias voltage breakdown threshold above 60 kV/cm as well as a higher optical pump saturation point.<sup>58</sup> The broadband THz performance of GaAs:As $^{3+}$  was characterized as a detector in a TDS configuration, where a 15-fs optical pump was used to excite a ZnTe crystal emitter and generate broadband (47 THz) pulses, as well as gate the GaAs-based detectors.<sup>59</sup> Comparing GaAs:As $^{3+}$ , SI-GaAs, and LT-GaAs, it was found that SNR and bandwidth was greatest for the LT-GaAs detector (>40 THz bandwidth) due to the comparably short carrier lifetime, while the GaAs:As $^{3+}$  and SI-GaAs had lower bandwidths of 32 and 24 THz, respectively.<sup>59</sup> The noise was attributed to thermal noise in the photoconductor, arising from residual photocurrents. Therefore, Liu et al.<sup>59</sup> proposed that the noise in the GaAs:As $^{3+}$  emitter could be reduced by increasing the ion-implantation depth, as this would effectively increase the effective carrier mobility while retaining a short carrier lifetime.

Salem et al. compared THz PCAs based on arsenic,<sup>60,61</sup> hydrogen (GaAs:H $^+$ ),<sup>60,62</sup> oxygen (GaAs:O $^{2-}$ ),<sup>60,61</sup> and nitrogen (GaAs:N $^{3-}$ )<sup>60</sup> ion implantation. Lowest THz pulse intensity was observed in the GaAs:N $^{3-}$  PCA, while the GaAs:H $^+$ , GaAs:As $^{3+}$ , and GaAs:O $^{2-}$  demonstrated comparable output THz intensities when operated in the saturation regime of the optical pump power (90 mW).<sup>60</sup>

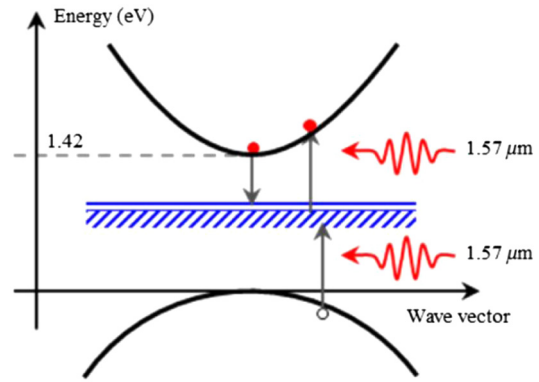


**Fig. 7** Schematic of two-step 1.57- $\mu\text{m}$  photon absorption process enabled by midgap states in arsenic-rich LT-GaAs.<sup>114</sup> Reprinted with permission from Ref. 114. Copyright 2015 American Chemical Society.

Use of GaAs:H $^+$  as both the emitter and receiver was demonstrated in a TDS configuration to provide a SNR nearing  $10^4$  from 0.1 to 1 THz.<sup>62</sup> Although the work by Salem et al.<sup>60</sup> indicated poor relative performance in GaAs:N $^{3-}$ , this material was shown by Winnerl et al.<sup>63</sup> to have 40 times better SNR than SI-GaAs based detectors, and nearly the same SNR of LT-GaAs. Additionally, GaAs:N $^{3-}$  PCAs operating in a photomixing configuration have been shown to have a higher, bias independent cutoff frequency as compared to LT-GaAs, which exhibited decreasing cutoff frequency with increasing bias voltage.<sup>64</sup>

### 2.3 Indium Gallium Arsenide

In more recent years, the group III-V ternary compound indium gallium arsenide ( $\text{In}_x\text{Ga}_{x-1}\text{As}$ ) has been investigated as a potential candidate for THz PCA photoconductive material.<sup>69,87,93-99</sup> The benefit of this material is its potential to achieve 0.8 eV room temperature bandgaps, which allows for 1.55- $\mu\text{m}$  optical excitation. This is an advantage when considering practical implementation of THz PCA-based systems as 1.55- $\mu\text{m}$  wavelength pulsed laser systems can be fully fiber based without consideration of dispersion effects. Although generation and detection of THz pulses in LT-GaAs PCAs has been demonstrated using 1.55- $\mu\text{m}$  optical pulses,<sup>113,114</sup> a significant reduction in performance has been observed as compared to 800-nm excitation. This is mainly due to the lower absorption efficiency of LT-GaAs at 1.55  $\mu\text{m}$ , since absorption at this sub-bandgap wavelength requires interband transitions to excite carriers to the conduction band, as illustrated in Fig. 7 [Fig. 1(a) in Ref. 114].<sup>114</sup> Therefore, materials with bandgaps at or below 0.8 eV have been sought out for use with 1.55- $\mu\text{m}$  fiber laser systems.

As previously discussed, short-carrier lifetime photoconductors are needed to have the subpicosecond response necessary for THz generation and detection. For InGaAs, iron doping (InGaAs:Fe $^{2+}$ ) has been shown to provide the effective recombination sites needed for a subpicosecond carrier lifetime.<sup>69,87,93,97</sup> Suzuki and Tonouchi demonstrated reduction of the emitted THz pulse from 0.68 to 0.57 ps in InGaAs PCA emitters due to Fe $^{2+}$  implantation under identical operating conditions.<sup>93</sup> Additionally, InGaAs:Fe $^{2+}$  demonstrated higher optical pump saturation power as well

as higher breakdown voltage, indicating further improvement in performance at higher operating conditions.<sup>93</sup> Utilized as a detector, annealing at 580°C was shown to improve the detection SNR from 50 to 133.<sup>87</sup> Metalorganic chemical vapor deposition grown InGaAs:Fe<sup>2+</sup> was investigated across 830-nm to 1.55- $\mu$ m optical excitation as an emitter by Wood et al.<sup>69</sup> and later as a detector by Hatem et al.<sup>97</sup> As emitters, highest THz power of 9  $\mu$ W was observed around 1.2- $\mu$ m excitation wavelength.<sup>69</sup> As detectors, peak SNR of 125 was observed at 5-mW optical excitation with bandwidth limited by the excitation pulse width.<sup>97</sup> MBE grown nanoparticle embedded InGaAs was studied by Salas et al.<sup>98</sup> and Murakumo et al.<sup>99</sup> InGaAs based nanocomposites containing rare-earth arsenide nanospheres were proposed as a possible material for THz PCAs.<sup>98</sup> Of the four materials studied, lanthanum arsenide (LaAs) had over an order of magnitude higher dark resistivity and three times lower mobility as compared to erbium arsenide (ErAs), lutetium arsenide (LuAs) and gadolinium arsenide (GdAs) under similar growth conditions.<sup>98</sup> Use of InAs:Er<sup>3+</sup> quantum dot embedded InGaAs has been shown to provide higher optical saturation intensity, an attractive property for high power THz emitters.<sup>99</sup>

#### 2.4 Indium Gallium Arsenide/Indium Aluminum Arsenide (InGa(Al)As) Heterostructures

InGa(Al)As multi-quantum wells (MQWs) and superlattices have been proposed as potential materials for THz PCAs.<sup>100–107</sup> Similar to bulk InGaAs, InGa(Al)As can achieve strong optical absorption under 1.55- $\mu$ m wavelength excitation, due to its tunable bandwidth. However, unlike bulk InGaAs, the highly tunable electro-optic properties of InGa(Al)As have been proposed as an avenue to achieve equivalent (or better) THz PCA performance at 1.55  $\mu$ m that LT-GaAs achieves at 800 nm.<sup>115</sup> Although earlier works proposed InGa(Al)As-based materials for THz PCAs,<sup>100,116</sup> the first InGa(Al)As-based THz PCA operating at 1.5  $\mu$ m was demonstrated by Sartorius et al.<sup>115</sup> Alternating layers of 12 nm InGaAs:Be<sup>2+</sup> and 8 nm InAlAs were grown on InP wafers to form the PCA substrate. An illustration of this configuration, showing the separate embedded photoconductor, electron trapping layer, and combined multilayer structure, is shown in Fig. 8 (Fig. 4 in Ref. 115).<sup>115</sup> The InGaAs:Be<sup>2+</sup> acted as the photoconducting region and was grown using standard low temperature methods for bulk InGaAs; however, incorporation of Be<sup>2+</sup> during growth allowed the material dark resistivity to be increased by balancing against the As<sup>3+</sup> antisites.<sup>115</sup> To further increase the net dark resistivity and decrease carrier lifetime, the InAlAs layers were included. This material had a higher dark resistivity than the InGaAs:Be<sup>2+</sup> and acted as a deep level trapping site for electrons.<sup>115</sup> Conventional THz PCA electrodes were fabricated on these materials to form both emitters and detectors, which were then incorporated into an all fiber THz TDS experimental setup. Sub-1 ps THz pulses with bandwidth extending above 2 THz were reported along with a SNR of nearly 3 orders of magnitude.<sup>115</sup> Other works have elaborated on this concept to further study this material's potential for all fiber THz TDS systems.<sup>101–107</sup>

Roehle et al.<sup>102</sup> utilized InGa(Al)As multilayers and employed a mesaetching process to effectively increase the generated photocurrent while decreasing dark current.

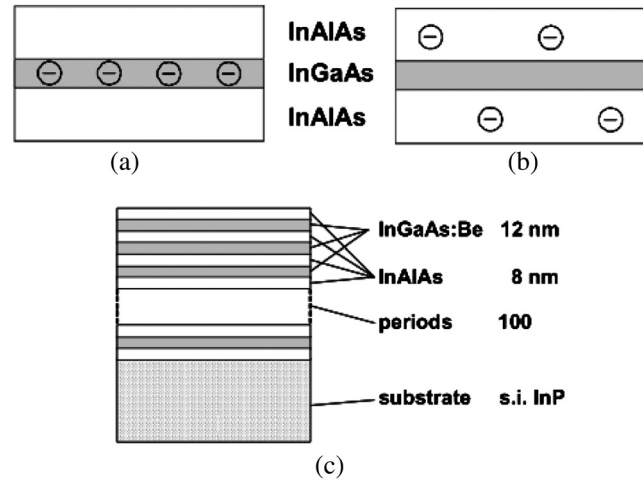


**Fig. 8** (a) Embedded photoconductor; (b) electron trapping; and (c) multilayer structure. Reprinted from Ref. 115 with permission from OSA Publishing.

This led to a 27.5 $\times$  increase in detected THz amplitude as compared to a nonmesa PCA.<sup>102</sup> Other demonstrations of InGa(Al)As multilayer-based THz PCAs have attempted to further optimize growth conditions, which are critical for maximum THz performance.<sup>103,105–107</sup> Using a mesa-style emitter with 2 nm InAlAs barriers and 400°C InGaAs growth temperature with no doping, high THz output powers of 64  $\mu$ W were achieved at 32-mW optical excitation.<sup>107</sup> Additionally, erbium arsenide (ErAs) quantum dot incorporation into the InAlAs trapping layers has been studied and shown to provide up to 1 V/cm amplitude THz pulses at 100-mW excitation wavelength.<sup>104</sup> The most recent work by Dietz et al.<sup>117,118</sup> has shown optimal growth conditions for 1060-nm excitation along with a further study of optimized Be<sup>2+</sup> doping for 1.55- $\mu$ m excitation detectors. Over 6-THz detection bandwidth and 90-dB dynamic range was reported for detectors fabricated on InGa(Al)As multilayers with Be<sup>2+</sup> doping concentrations of  $4 \times 10^{18}$  cm<sup>-3</sup>.<sup>118</sup>

#### 2.5 Other Group III-V Materials

Although GaAs and InGa(Al)As are the most widely studied material systems for THz PCA development, several other group III-V materials have been investigated as well.<sup>66,108–111,119,120</sup> THz emission in antimony (Sb) based materials, such as InSb,<sup>108</sup> GaAsSb,<sup>109</sup> GaSb,<sup>119</sup> and GaInSb,<sup>120</sup> has been studied by several groups, although only the work of Sigmund et al.<sup>109</sup> fabricated and characterized THz PCAs on the material. 1-THz bandwidths were observed in a THz TDS system utilizing GaAsSb material in the PCA emitter and detector, although more study of the growth conditions is needed to fully evaluate the potential of this material for THz PCAs.<sup>109</sup> GaBiAs was grown at two different temperatures and used for THz PCA fabrication by Bertulis et al.<sup>110</sup> Four times higher THz field amplitudes were observed in a 330°C grown sample as compared to a 280°C growth.<sup>110</sup> GaAs embedded superlattices of rare-earth arsenides of ErAs and LuAs were used in CW photomixing in plasmonic PCAs.<sup>66</sup> In all cases, the rare-earth arsenide-based photomixers outperformed LT-GaAs photomixers at operation frequencies below 1 THz, though output power

**Table 1** Summary of photoconductive material development for THz PCAs.

	Advantages	Disadvantages	Key reported performance milestones
GaAs	Most efficient material for 800 nm excitation Well understood growth and optimization	Poor absorption at 1.55 $\mu\text{m}$	$10^4$ SNR <sup>62</sup> 60 kV/cm breakdown threshold <sup>58</sup>
InGaAs	1.55- $\mu\text{m}$ excitation	Decreased gap dark resistivity	10- $\mu\text{W}$ output THz power <sup>69</sup> 125 SNR <sup>97</sup>
InGa(Al)As heterostructures	1.55- $\mu\text{m}$ excitation comparable dark resistivity to LT-GaAs	Complex material growth	$10^3$ SNR <sup>115</sup> 6-THz bandwidth <sup>118</sup> 1-V/cm THz amplitude <sup>104</sup>
Other group III-V	Potential 1.55 $\mu\text{m}$ excitation	New materials with limited understanding	1 THz bandwidth, $10^2$ SNR (GaAsSb) <sup>109</sup>

was higher in LT-GaAs for higher frequencies.<sup>66</sup> Collier et al.<sup>111</sup> fabricated THz PCAs on InP to study the effects of surface roughness on the THz emission. Although surface roughness showed no effect on the amplitude and bandwidth of THz emission, around 1 order of magnitude suppression of the photocurrent was observed.<sup>111</sup> This indicated that such emitters could have higher operation thresholds as compared to nontextured materials, allowing for enhanced THz performance.<sup>111</sup>

## 2.6 Summary and Outlooks

The advantages, disadvantages, and key performance milestones for each of the material systems discussed are summarized in Table 1. Although LT-GaAs remains the standard for THz PCAs, the potential for all fiber-based TDS systems remains an attractive motivator for investigating and developing other photoconductive materials systems. Remaining challenges for lower bandgap THz PCA materials include reaching comparable (or better) carrier lifetime, mobility, breakdown threshold, quantum efficiency, and reproducibility to that of standard LT-GaAs devices.

## 3 Large Area Emitters

### 3.1 Challenges

One of the major limiting factors of THz PCA technology is saturation at high optical pump powers.<sup>55,77,83,121,122</sup> Under no optical illumination, the photoconductor has a fixed carrier concentration  $N_D$  or  $N_A$ , where  $N_D$  is the donor carrier concentration and  $N_A$  is the acceptor carrier concentration.<sup>112</sup> Illuminating the photoconductor induces an optical carrier concentration,  $N_{\text{opt}}$ , which induces an increase in the total carrier concentration of  $N_{\text{tot}} = N_{D,A} + N_{\text{opt}}$ . Changes in the material carrier concentration translate to a proportional change in electronic properties, namely the imaginary part of the permittivity. For optical pump powers, where  $N_{\text{opt}} \geq N_{D,A}$ , the imaginary part of the permittivity will begin to increase, causing a nonlinear increase in the surface reflectivity of the air-photoconductor interface.<sup>122</sup> Therefore, during operation of high optical pump power beyond the  $N_{\text{opt}} \geq N_{D,A}$  region, the output THz power will experience a nonlinear increase, eventually reaching a saturation point, where increasing optical pump power produces little to no increase in output THz power.<sup>122</sup> This effect is exaggerated as the optical pump is focused to a smaller spot size.<sup>83,121</sup>

### 3.2 Large Aperture Dipoles

Overcoming the saturation limits of PCAs has been demonstrated through the implementation of large device apertures. This was first observed in the early 1990s by the research efforts of THz pioneer David Auston.<sup>79,83,121,123,124</sup> These PCAs consisted of parallel microstrip line dipole antennas with gaps ranging from 130  $\mu\text{m}$  to 4 mm. Various materials, including SOS,<sup>79,83,123</sup> InP,<sup>79,83,121</sup> and GaAs,<sup>79,83,121,124</sup> have been considered for use in these devices. Although initial work utilized large aperture PCAs to demonstrate THz beam steering,<sup>79,123</sup> it was noted that these devices have the added benefit of improved power scaling due to reduction of the saturation effect.<sup>121,123</sup> Extensive theoretical and experimental work was later performed to fully understand the saturation characteristics.<sup>83</sup> The emitted THz pulses were measured in a TDS configuration to obtain the relationship between emitted pulse amplitude and incident optical fluence. InP- and GaAs-based emitters were found to have similar THz amplitudes, around twice that of SOS emitters. In all cases, the large aperture emitters were shown to generate emitted THz pulses with peak amplitude electric field values within 90% of the DC bias field value.<sup>83</sup>

Later works have further studied the properties of large aperture THz PCAs.<sup>56,67,77</sup> Benicewicz, Roberts, and Taylor fabricated 500- $\mu\text{m}$  gap microstrip dipoles on InP:Fe<sup>2+</sup> and SI-GaAs and studied their saturation properties in a THz TDS experimental configuration.<sup>77</sup> A comparison of the radiated electric field for devices fabricated along different crystallographic axes showed only slight variation. This variation was unable to be described by the theoretical model and was attributed to variation in the material properties across the wafer, not the specific crystal orientation.<sup>77</sup> The radiated THz power as a function of optical fluence and bias voltage was measured, with excellent agreement being observed with the proposed theoretical model.<sup>77</sup> Budiarto et al.<sup>67</sup> studied the effects of AC biasing of a GaAs-based THz PCA with 3-cm electrode gaps. The emitted THz pulse intensity was measured as a function of optical fluence for two different emitter AC bias frequencies, 0.1 and 1 kHz, and four different bias voltage amplitudes. In all instances, the 1-KHz bias frequency increased the intensity of the emitted THz in the saturation regime.<sup>67</sup> At the highest observed bias field of 6 kV/cm, no saturation was observed for optical fluence up to 90  $\mu\text{J}/\text{cm}^2$ .<sup>67</sup> Large aperture emitters were studied as well by Stone et al.,<sup>56</sup> although the laser utilized in this study was not powerful enough to provide the high optical fluence necessary to observe saturation effects.

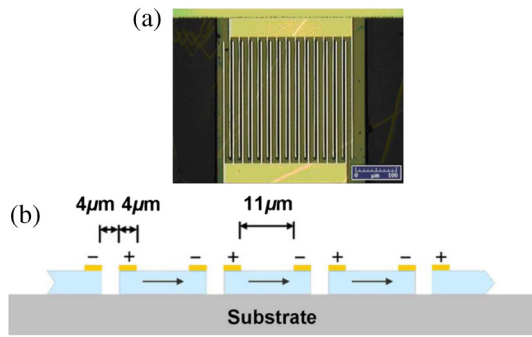


**Fig. 9** (a) Micrograph of terahertz array antenna device. (b) Cross-sectional view of terahertz antenna array. Reprinted from Ref. 131, with permission of AIP Publishing.

### 3.3 Interdigitated Electrodes

Similar to large aperture dipoles, attempts to overcome the saturation limits of conventional THz PCAs have investigated increasing the device active area by implementing interdigitated electrodes.<sup>63,71,80,84,106,125–135</sup> This configuration consists of a single anode and cathode, each connected to a number of open ended parallel microstrips. The anode and cathode microstrips were interwoven, so the space between two adjacent anode microstrips was occupied by a cathode microstrip, and vice versa, with a fixed gap distance between the two electrodes. An illustration and device photograph of this configuration is shown by Awad et al. in Fig. 9 (Fig. 1 in Ref. 131).<sup>131</sup> By this method, active areas of a few hundred  $\mu\text{m}^2$  have been produced, allowing the optical power to be spread over a larger area to reduce the saturation effect.<sup>128</sup> Unlike large aperture PCAs, interdigitated PCAs have the added benefit of enhancing the near anode effect.<sup>127</sup> By reducing the saturation effects, these electrode configurations have shown promise for providing high optical to THz conversion efficiency even at high optical pump powers.

Interdigitated electrodes for improved performance in THz PCA photomixers were proposed by several groups in the early 1990s.<sup>125–127</sup> The first truly broadband photomixer implementing interdigitated electrodes for THz generation up to 3.8 THz was demonstrated in 1995 by Brown et al.<sup>128</sup> Using a log spiral antenna with 1.8- $\mu\text{m}$  gap interdigitated electrodes, a maximum output power of 10  $\mu\text{W}$  was observed at a 0.3-THz operational frequency, with measurable radiation up to 3.8 THz reported.<sup>128</sup> Brown<sup>84</sup> later developed a model for predicting the performance of an interdigitated THz photomixer. Here, it was proposed that by implementing a reflecting layer under the LT-GaAs and tuning the thickness of the LT-GaAs cavity, the absorption of the incident optical pump could be optimized. This increased the output THz power by a factor of 7 due to improved quantum efficiency of the device.<sup>84</sup> Later work by Gregory et al.<sup>80</sup> extensively studied THz PCA photomixers with varied interdigitated electrodes. Photomixers with 3, 5, and 11 finger interdigitated electrodes were fabricated and characterized under CW and pulsed operation. Spatial mapping of the emitted THz radiation as a function of location of a focused optical excitation was performed for an 11 finger device. The results showed no enhancement of THz emission when focused at the electrode tips, as well as no near anode enhancement effects. For CW operation, the larger active region provided by a larger number of electrode

fingers did not provide enhanced THz emission. At higher THz frequencies above 0.4 THz, the increased capacitance led to a high frequency roll off in the device performance. However, at sub-0.4 THz operation, a larger device active area could provide advantages of more efficiency heat dissipation and reduced sensitivity to beam drift.<sup>80</sup>

Many others have utilized interdigitated electrodes in various THz PCA designs for pulsed operation.<sup>63,104,106,129,132,136,137</sup> Dreyhaupt et al.<sup>129</sup> proposed a novel modification to the interdigitated electrode design to overcome an inherent limitation of this configuration. In standard interdigitated electrodes, the bias electric field direction is rotated 180 deg between adjacent gaps. The carriers generated accelerate in opposing directions, leading to a net destructive interference in the emitted electromagnetic field. By incorporating a shadow mask, which blocks the incident optical excitation in every other gap, photogeneration only occurs in regions with the same bias field directions. This leads to a net constructive interference, providing high intensity THz pulse emission up to 85 V/cm.<sup>129</sup> This was expanded upon in later works, including demonstration of an interdigitated PCA for THz detection using an unfocused optical gating pulse,<sup>132</sup> study of the dependence of generation and detection performance on GaAs carrier lifetimes<sup>63</sup>, and emission of 2.5 V/cm THz pulses in InGaAs heterostructure emitters under 1.55- $\mu\text{m}$  wavelength optical excitation.<sup>106</sup> All works indicate that improved performance was achieved by implementation of the interdigitated large active area.<sup>63,104,106,129,132,136,137</sup>

Hattori et al.<sup>130</sup> characterized a seven-element array of larger area interdigitated electrode emitters. This was compared to emitter arrays of noninterdigitated large area emitters comprised of parallel microstrips with 3-cm gaps. This configuration is illustrated in Fig. 10 (Fig. 1 in Ref. 130). Here, it was found that the noninterdigitated array produced nearly two times greater peak THz emission, although they require 6-kV bias voltage to achieve the same gap bias field as the interdigitated emitter under 30-V bias voltage.<sup>130</sup> Others have implemented shadow masks for interdigitated PCAs,<sup>71,134,135</sup> with reports of 20 THz ultrabroadband performance under collinear operation<sup>135</sup> and high pulsed operation average powers of 3.8 mW.<sup>71</sup> Awad et al.<sup>131</sup> presented an alternative method for preventing the destructive interference occurring in nonshadowed interdigitated PCAs. Here, rather than blocking the incident optical pulse, the photoconductive material in every other gap of the device was etched away. In addition to preventing destructive interference, this has the added benefit of allowing the active area of the device to be increased since the etched region gaps can be reduced while still allowing the majority of the electric field to fall in the nonetched gaps.<sup>131</sup> A similar device configuration was studied by Acuna et al.,<sup>133</sup> which demonstrated peak THz fields of 15 V/cm and 40,000  $\text{Hz}^{1/2}$  SNR under electro-optic sampling.

### 3.4 Dipole Arrays

Periodic arrays of dipole electrodes have been proposed for improving various aspects of THz PCA performance.<sup>124,138–141</sup> Early work by Froberg et al.<sup>124</sup> fabricated a linear array of parallel microstrip dipole emitters on SI-GaAs. Each of the 64 electrodes was individually biased, while the entire array was illuminated with a train of 200-fs optical pulses. It was shown that by controlling the bias of the individual

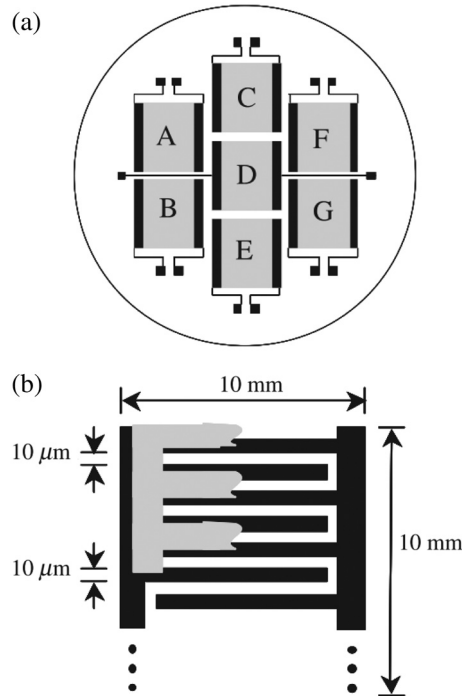


**Fig. 10** (a) Schematic of THz emitter composed of seven photoconductive antenna units having interdigitated electrode structure. The units are labeled A–G for later reference. (b) Structure of electrodes and shadow mask of each unit.<sup>130</sup> Copyright 2006 The Japan Society of Applied Physics.

electrodes, the direction and profile of the emitted THz pulses could be tuned.<sup>124</sup> Various works by Klatt et al.<sup>138,139</sup> studied electrode arrays utilizing the photo-Dember effect for THz generation. The photo-Dember effect arises from the optically induced space-charge gradient in unbiased semiconductors due to the difference in electron and hole diffusion coefficients.<sup>138</sup> This effect was shown to be enhanced near the edge of an unbiased metal electrode,<sup>138</sup> with photo-Dember excitation of electrode arrays showing comparable THz generation as interdigitated PCA emitters.<sup>139</sup> Berry et al.<sup>140</sup> fabricated a  $3 \times 3$  array of log spiral antennas with nanoscale plasmonic electrodes. Using an array of optical microlenses, the incident optical pump was divided into nine separate beams and focused onto the active area of each device. The net output THz radiation was shown to reach record high-average power levels of 320 mW at an average pump power of 1.9 mW.<sup>140</sup> Microlens arrays were also utilized by Singh and Prabhu<sup>141</sup> to excite the individual active areas of an interdigitated THz

PCA emitter. The microlens array was utilized to divide and control the location of the excitation, so only regions leading to constructive interference were excited, rather than utilizing a shadow mask or etching the photoconductor in these regions.<sup>141</sup>

### 3.5 Summary and Outlooks

The advantages, disadvantages, and key performance milestones for large area emitter THz PCAs are summarized in Table 2. These devices offer a potential for drastically increasing the optical-to-THz conversion efficiency, which is necessary for high output THz power or efficient excitation of multiple devices with a single-laser source. However, as the device active area increases, the driving current can no longer be considered a point source, leading to potential phase interference issues not present in single dipole emitters. Additionally, most large area emitters have complex fabrication and/or packaging considerations. As solutions to these problems continue to be sought out, large area emitters will likely develop into standard THz PCA technology.

## 4 Plasmonic Nanostructures

### 4.1 Challenges

Several groups have studied the use of plasmonic nanostructures in both THz PCA emitters as well as receivers. Similar to large-area emitters, nanostructures attempt to more efficiently utilize the incident optical pump. As previously discussed, THz generation in conventional PCAs occurs mainly due to the photocarriers that are generated in the high bias field region (i.e., at the surface) and near the antenna anode.<sup>80,85</sup> However, in conventional PCAs, only a small fraction of the incident photons is absorbed near the surface, with even less being absorbed in a region near enough to the antenna anode for the generated carriers to be collected on a subpicosecond time scale. This translates to a distance of around 100 nm or less from the antenna anode.<sup>76</sup> As an example, consider an 800-nm wavelength,  $5\text{-}\mu\text{m}$  diameter optical beam focused in the gap of a LT-GaAs THz PCA centered over the anode edge. Anode illumination has been shown to generate the highest levels of THz power, as compared to the middle of the gap of cathode illumination.<sup>85</sup> Here,  $<2\%$  of the total photons is incident in a lateral distance 100 nm or less from the antenna anode, and only around 13% of these are absorbed in the first 100-nm depth of the LT-GaAs. Therefore, considering only THz generation from the carriers that are collected by the anode,  $<0.3\%$  of the incident photons are theoretically able to contribute to THz generation. The remaining photons are lost either by

**Table 2** Summary of large area emitter THz PCAs.

	Advantages	Disadvantages	Key reported performance milestones
Larger aperture dipoles	Reduced saturation effects	Order of magnitude higher bias voltage required	No saturation up to $90 \mu\text{J}/\text{cm}^2$ optical fluence <sup>67</sup>
Interdigitated electrodes	Reduced saturation effects	Increased fabrication complexity and unable to incorporate broadband antenna designs	15 to 85 V/cm THz amplitude <sup>129,133</sup>
Dipole arrays	Reduced saturation effects	Increased optical alignment complexity	1.9-mW output THz power <sup>140</sup>

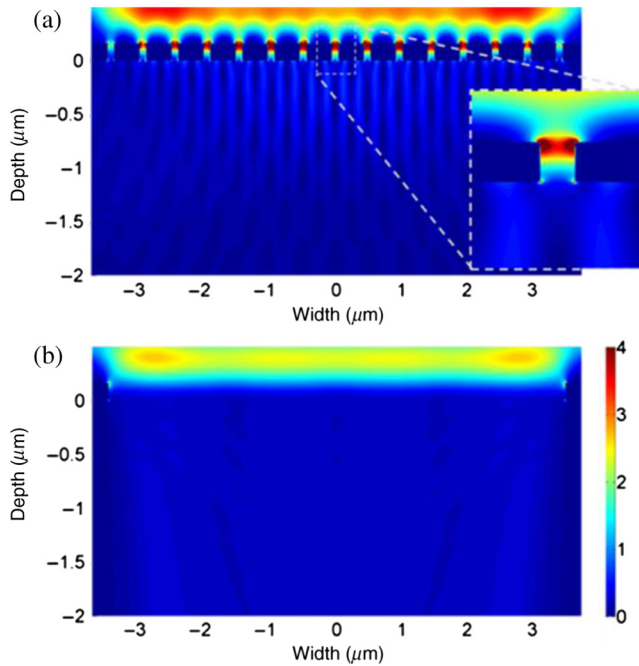


**Fig. 11** Cross-section of plasmonic enhancement showing local intensity increase. (a) PE-LT-GaAs and (b) LT-GaAs. Reprinted from Ref. 114. Copyright 2015 American Chemical Society.

reflection from the anode metallization or are absorbed too far ( $>100$  nm) from the anode to be collected before recombining.<sup>76</sup>

Plasmonics have been proposed as a viable solution for overcoming this inherent limitation in conventional THz PCA design. “Plasmonics” refers to the study of the collective electron oscillations that occur in subwavelength sized metallic nanostructures when excited by an external optical wave.<sup>142</sup> These oscillations have been shown to enhance the optical near field by orders of magnitude, with the oscillation frequency, magnitude, and spatial location of the enhancement being tunable by the size, shape, and surrounding medium of the nanostructures.<sup>143–145</sup> Plasmonics have been proposed and demonstrated extensively in solar cell technology.<sup>143–147</sup> Plasmonic enhancement of THz PCAs follows a similar approach, where the nanostructures are designed to enhance the optical excitation field in regions inside the photoconductive material where the generated carriers most efficiently convert to output THz radiation. This is illustrated in the computational modeling work of Jooshesh et al., shown in Fig. 11 (Fig. 4 in Ref. 114). Here, the optical field at the THz PCA gap is shown for cases with (PE-LT-GaAs) and without (LT-GaAs) plasmonic nanostructures located at the LT-GaAs surface. It is shown that the plasmonic structures enhanced the local optical field at the LT-GaAs surface.<sup>114</sup>

#### 4.2 Early Examples of Unbiased Nanostructured Terahertz Emitters

The first examples of using metal nanostructures for THz generation were not incorporated into PCAs. Instead, THz was generated through a process called “optical rectification.”<sup>4,5,148–150</sup> Similar to PCA generation, optical rectification uses a subpicosecond optical pulse to excite an unbiased semiconductor, electro-optic crystal, or metal

surface. The optical field induces oscillations in the material, which follow the intensity envelope of the pulse rather than the electric field. These oscillations in the material then re-emit as a propagating THz pulse.<sup>5</sup> Although optical rectification using unbiased semiconductors and electro-optic crystals has existed nearly as long a PCA technology,<sup>44</sup> the first demonstration of THz generation from a nanostructured metal surface did not take place until 2006.<sup>151</sup> This early work of Welsh and Hunt<sup>151</sup> studied THz surface emission from nanostructured metal surfaces excited by 800-nm wavelength optical pulses. Here, it was found that the nanostructured metal surfaces had much higher optical-to-THz conversion efficiency than flat metal surfaces. However, the peak THz field from the nanostructured metal surface was still around 1 order of magnitude lower than the peak field emitted from a zinc telluride (ZnTe) electro-optic crystal. Additionally, it was found that the THz-optical power dependence did not follow a quadratic dependence expected from optical rectification alone. Instead, the power dependence followed an  $x^{3.4}$  behavior, indicating other processes such as surface plasmon excitation.<sup>151</sup> This work was the first evidence that THz generation utilizing plasmonic nanostructures could be possible.

Several later works continued to explore THz emission from metallic nanostructured surfaces.<sup>152–156</sup> Welsh and Wynne expanded on their initial work by studying a periodic nanoscale grating structure etched into fused silica and coated in a thin metal layer. Characterization of the optical absorption spectrum showed a narrow absorption peak characteristic of plasmonic resonance. This peak could be tuned from around 670 to 870 nm central wavelength across a 20- to 50-deg incident angle range.<sup>153</sup> For gratings coated in a 40-nm gold (Au) layer, the maximum output THz field was around 50% lower than the field generated from a 0.5-mm thick ZnTe crystal. When coated in 45 nm of silver (Ag), however, the THz field dropped to over 2 orders of magnitude lower.<sup>153</sup> Theoretical studies by Gao et al.<sup>154</sup> investigated ordered arrays of metal nanodisks, rings, and pyramids on a glass surface. The intensity of THz radiation emitted from these surfaces was shown to be highly dependent on the nanostructure geometry, although geometry did not alter the bandwidth of the emitted THz.<sup>154</sup>

Extensive experimental work by Polyushkin et al.<sup>155</sup> utilized nanosphere lithography techniques to fabricate triangular nanostructure arrays and study their THz emission characteristics. Similar to previous works, it was found that the intensity of the output THz pulses was highly dependent on the size and shape of the nanostructures. Although the output THz intensity was around 10× lower than a standard ZnTe crystal, it was noted that certain applications could take advantage of the extremely thin (submicron) nature of these nanoplasmonics emitters.<sup>155</sup> Ramakrishnan et al.<sup>156</sup> compared randomly nanostructured metal films to continuous ones, observing up to 24× enhancement of output THz intensity as compared to continuous films. However, it was noted that the highest THz intensities observed were still nearly 2 orders of magnitude lower than conventional THz PCA emitters.<sup>156</sup> Further work by Ramanandan et al.<sup>157</sup> demonstrated that absorption in the region near the Schottky junction of the device is critical for THz generation, more than the total amount of light absorbed. This configuration is illustrated in Fig. 12(a) [Fig. 1(a) in Ref. 157], where the

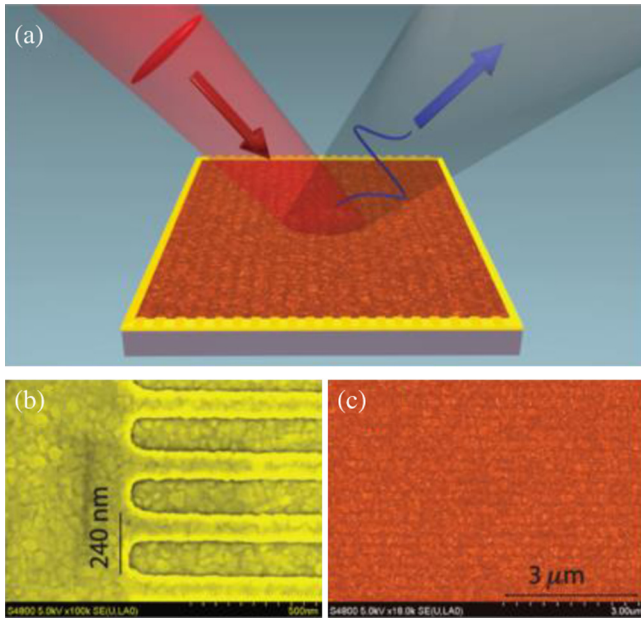


**Fig. 12** (a) Schematic diagrams of the nanostructured Au/Cu<sub>2</sub>O Schottky junction THz emitter. The pump laser pulses are incident on the sample, generating THz pulses. A nanograting is fabricated at the interface to facilitate the excitation of surface plasmons. (b, c) False-color SEM image of the grating after the deposition of Au and Cu<sub>2</sub>O, respectively. Reprinted with permission from Ref. 157. Copyright 2014 American Chemical Society.

THz surface emission is enhanced by the optical interaction with the nanograting surface plasmons. Scanning electron microscope (SEM) images of the fabricated device before and after cuprous oxide (Cu<sub>2</sub>O) deposition are shown in Figs. 12(b) and 12(c) [Figs. 1(b) and 1(c) in Ref. 157].<sup>157</sup>

Several uniform conclusions can be drawn from the works studying THz emission from nanostructured metal surfaces. First, the generated THz oscillations are a direct result of the plasmon oscillations in the nanostructures. Second, there is a strong dependence on the intensity of the output THz on the magnitude of the nanostructure plasmon resonance. Third, the intensity of the emitted THz is generally 1 order of magnitude lower than that of a ZnTe crystal, though the drastically reduced thickness of the emitter could provide advantages in certain applications. Although the previously described works presented THz generation through unbiased optical-plasmon interactions alone, they were inspiration for later works combining nanoplasmonics and PCA technology for producing high-power pulsed THz sources.

### 4.3 Gap-Located Nanostructures

The first demonstration of enhanced THz PCA performance through incorporation of plasmonic nanostructure arrays was given in 2011 by Park et al.<sup>158</sup> Standard bowtie dipole antennas were patterned on SI-GaAs substrates, followed by electron beam lithography patterning of periodic nanostructure arrays in the dipole gap. Four different configurations were compared: two nanosquare arrays and two nanograting arrays with 75- and 150-nm widths. Reflectance measurements illustrated minimum reflectance in the 75-nm nanosquares at an 800-nm excitation wavelength. Comparing the nanostructured PCAs to conventional ones, it was found that the greatest improvement in output THz power was

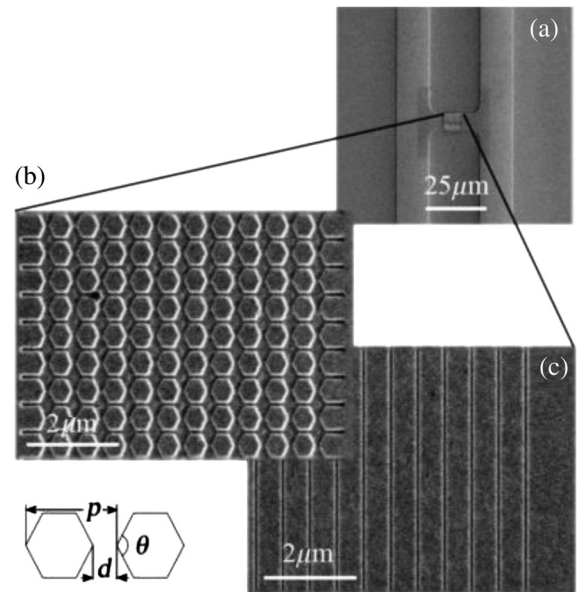


**Fig. 13** (a) SEM image of the 20- $\mu$ m dipole on SI-GaAs substrate. (b) The active area of the hexagonal plasmonic array. (c) The active area of the strip plasmonic array. The diagram shows apex angle  $\theta$ , gap size  $d$ , and periodicity  $p$ . Reprinted from Ref. 161 with permission from OSA Publishing.

observed in the 75-nm nanograting arrays, which increased the 0.1- to 1.1-THz average power by a factor of 2.27.<sup>158</sup> The work was continued by Park et al.,<sup>159,160</sup> where the electron beam lithography was replaced with an annealing process to self-assemble Ag nanoislands; additionally, the previously studied nanogratings<sup>158</sup> were further optimized to improve THz emission. The self-assembled Ag nanoislands showed 0.1 to 1.1 THz average power enhancement by a factor of 2, lower than the nanograting studies.<sup>158</sup> Measurements of the optical spectrum extinction coefficient of the array were compared to measured output THz power of the array for varied nanograting width.<sup>160</sup> It was found that when the peak in the extinction coefficient centered at the 800-nm excitation wavelength, the output THz power enhancement across the 0.1 to 1.1 THz range was maximized at  $2.4\times$ .<sup>160</sup>

Others have incorporated gap-located nanostructures into THz PCAs to improve aspects of the device performance. Jooshesh et al.<sup>161</sup> fabricated PCAs with ordered arrays of hexagonal and grating nanostructures in the antenna gap, as well as a reference conventional nonplasmonic dipole emitter, all on SI-GaAs. SEM images of the fabricated devices are shown in Fig. 13 (Fig. 1 in Ref. 161). Comparing the plasmonic structures to the conventional reference, it was found that the hexagonal structures had the greatest enhancement of the THz pulse peak at a factor of around 5.5 at an optical pump power of 2 mW.<sup>161</sup> Further work exploited an additional advantage of gap-located plasmonic nanograting structures.<sup>114</sup> Here, it was demonstrated that these plasmonic structures could enable efficient absorption of photons with energy significantly below the bandgap of LT-GaAs. Exciting different PCAs with 1.57- $\mu$ m wavelength femtosecond pulses, it was shown that LT-GaAs based PCAs with the nanograting structures produced THz pulses with peak amplitude over 11 times greater than a conventional LT-GaAs PCA. Even more significant was that the peak THz field of the plasmonic LT-GaAs PCA was around 1.8 times

greater than that of a commercially available conventional PCA based on InGaAs, which had a bandgap below the excitation wavelength.<sup>114</sup> This enhanced performance was attributed to the introduction of midgap states in the LT-GaAs due to the presence of the plasmonic nanostructures. These midgap states allow for two photon absorptions to efficiently excite photocarriers from the valence to conduction band.<sup>114</sup> A unique architecture for a thin-film THz PCA detector was recently proposed by Mitrofanov et al.<sup>162</sup> This device consisted of a thin 280-nm LT-GaAs layer located between an AlAs/Al<sub>0.2</sub>Ga<sub>0.8</sub>As distributed Bragg reflector (DBR) and a periodic array of Au plasmonic nanostructures. The nanostructures and DBR worked in unison to effectively trap the incident photons in the LT-GaAs layer, increasing the optical absorption and generated photocarriers. The detectors showed a 50% increase in detected photocurrent when the nanostructures are included. This was achieved while maintaining a high dark resistivity of the device, which is necessary to minimize detection noise.<sup>162</sup>

#### 4.4 Nanostructured Electrodes

In addition to THz PCAs with gap-located nanostructures, several works have investigated nanostructuring of the antenna electrodes directly.<sup>66,71,72,76,140,163–166</sup> The key distinction here is that, in this configuration, the nanostructured regions are electrically continuous with either the anode or cathode, rather than being electrically isolated. An example of this from the work of Moon et al.<sup>167</sup> is shown in Fig. 14 [Fig. 1(a) in Ref. 167]. Here, a microscopic image of a standard dipole antenna structure is shown, along with SEM images of the various nanoplasmonic grating structures fabricated as part of the dipole electrodes.<sup>167</sup> Most work investigating nanostructured electrodes attempt to enhance the near-anode effect, the high output THz power that is observed when the optical pump is centered over the

anode. By nanostructuring the antenna electrodes, the effective area of the near-anode region can be increased, so the full area of the incident optical pump falls on the near-anode region. Additionally, the plasmonic resonances of the nanostructures can be tuned in such a way as to concentrate the incident optical pump in the near-field region of the anode, thus increasing the optical absorption inside the photoconductor near the anode. One of the first theoretical predictions of this effect was made by Zhong et al., where a narrow cone shaped anode fully embedded in a LT-GaAs layer was studied. Finite-difference time-domain (FDTD) studies illustrated that plasmonic enhancement of the optical field near the anode could be as high as 164 times greater in a nanoscale cone electrode as compared to a microscale cone electrode.<sup>163</sup>

Early fabrication and experimental demonstration of a THz PCA with nanostructured electrodes was performed in 2012 by Berry and Jarrahi.<sup>164</sup> Anode-ground-cathode dipole antennas were patterned on an In<sub>0.53</sub>Ga<sub>0.47</sub>As photoconducting layer, with a 1- $\mu$ m gap from the electrodes to the center ground and a 100/100 nm nanograting array incorporated into the electrodes.<sup>164</sup> These arrays, which were computationally studied in previous work,<sup>165</sup> increase the optical absorption, which takes place near the antenna electrodes.<sup>164</sup> Emitted THz pulsed from fabricated devices were shown to maintain a narrow 590-fs pulse width and generate average output THz power up to 5  $\mu$ W under 7-V bias and 85-mW optical power.<sup>164</sup> This concept was expanded on in several works.<sup>71,72,76,140,166</sup> Utilizing a 3  $\times$  3 array of log-periodic dipoles with nanograting electrodes, high average output THz power of 1.9 mW was demonstrated under a 320-mW optical pump power. These antennas, fabricated on LT-GaAs, required a microlens array for individual focusing of the incident optical pump onto the active area of each device.<sup>71</sup> The highest observed optical-to-THz conversion efficiency was demonstrated by designing a three-dimensional array of nanostructured electrodes.<sup>72</sup> In this example, the nanostructured electrodes consisted of rows of nanopillars etched into a LT-GaAs substrate with Au contact electrodes patterned on the sides and bottoms. These structures were shown to further localize the incident optical pump near the antenna anode and demonstrated a 7.5% optical-to-THz conversion efficiency at a 60-V bias and 1.4-mW optical pump power.<sup>72</sup> Utilizing the plasmonic nanograting design of Berry et al.,<sup>76,140</sup> a large area emitter was fabricated and demonstrated to produce a record high 3.8-mW average THz power across the 0.1 to 5 THz range.<sup>71</sup> This design has the advantage of not requiring alignment of a microlens array as in Ref. 140 as well as requiring comparatively less complicated fabrication methods for the plasmonic electrodes, as compared to Ref. 72.

Plasmonic nanostructured electrodes have been studied by several other groups as well.<sup>82,167–169</sup> Heshmat et al.<sup>168</sup> fabricated THz PCAs on LT-GaAs with interdigitated electrodes that had 100 nm anode-cathode gaps. The emitted THz pulse peak-to-peak amplitude was found to be 2 $\times$  greater than that of a commercially available conventional emitter. The improvement was even greater when compared to similarly shaped conventional emitters fabricated on LT-GaAs and SI-GaAs, which gave 10 $\times$  and 40 $\times$  improvement, respectively.<sup>168</sup> Tanoto et al.<sup>82</sup> fabricated and compared THz PCAs with tip-to-tip and interdigitated nanograting

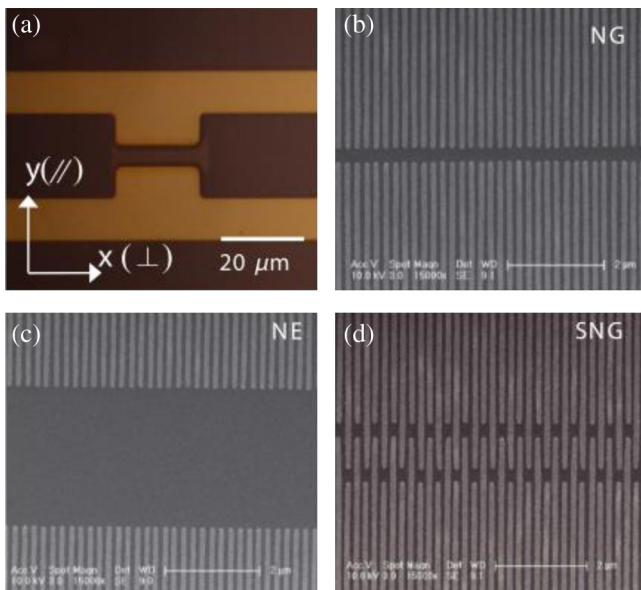


**Fig. 14** (a) Optical microscope image of H-dipole structure and (b–d) SEM of the fabricated nanostructures. Reprinted with permission from Ref. 167 under a Creative Commons Attribution 4.0 International License.

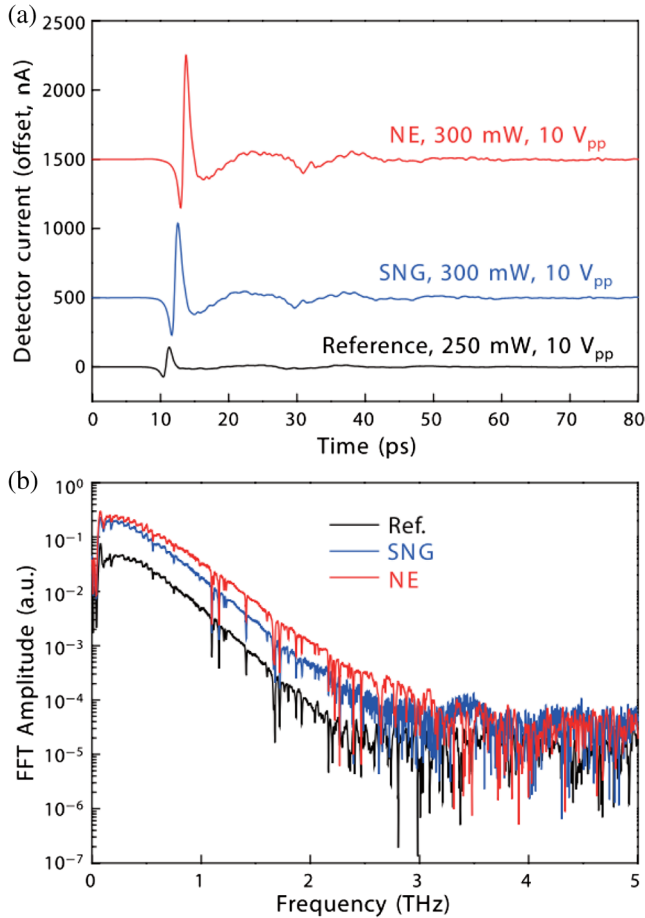


**Fig. 15** THz emission from the large-aperture PCAs: (a) time-domain curves and (b) FFT spectra. Reprinted with permission from Ref. 167 under a Creative Commons Attribution 4.0 International License.

electrodes in a CW photomixing configuration. A bolometer was utilized to measure the output THz intensity as a function of optical beat frequency. It was found that the tip-to-tip configuration had around 2 orders of magnitude increase in the THz intensity as well as increased bandwidth. FDTD simulations supported these measurements, showing that the calculated optical field enhancement matched the out THz intensity enhancement.<sup>82</sup>

Moon et al.<sup>167</sup> experimentally compared three different nanograting designs: nanograting electrodes with 3  $\mu\text{m}$  and 200 nm anode–cathode gaps and nanograting electrodes with partially interdigitated nanogratings between the anode and cathode. All devices showed increased power output at low optical excitation power as compared to a reference, nonplasmonic PCA, as shown in the time-domain waveform

and fast Fourier transform spectra in Fig. 15 (Fig. 5 in Ref. 167). The enhancement was attributed to two mechanisms: plasmonic enhancement of the optical field near the electrodes and enhancement of the DC bias field near the electrodes. The dominating mechanism depended on the power of the incident optical pump, which indicated that nanogratings with the 3- $\mu\text{m}$  gap were dominated by plasmonic enhancement while the partially interdigitated nanograting electrode was dominated by bias field enhancement.<sup>167</sup> Computational work by Burford and El-Shenawee using COMSOL<sup>®</sup> Multiphysics proposed a thin-film PCA emitter utilizing metal nanodisk arrays to enhance the optical absorption in the photoconductor.<sup>170</sup> It was shown that the combination of the plasmonic structures and thin-film photoconducting layer effectively localized the optical absorption near the antenna anode, increasing the peak-induced photocurrent by nearly 3 orders of magnitude.<sup>170</sup>

#### 4.5 Summary and Outlooks

The advantages, disadvantages, and key performance milestones for plasmonic nanostructure THz PCAs are summarized in Table 3. Similar to the large area emitters, these devices offer potential for high-device quantum efficiency, with some devices combining nanostructured electrodes with large area emitter designs to yield record-high output THz power of 3.8 mW from a PCA device.<sup>71</sup> However, due to the lack of maturity in nanoscale lithography technology, fabrication of such ordered metallic nanostructures remains far more complex than standard THz PCA devices. This is exaggerated by the high sensitivity of the optical–plasmon interaction with the nanostructure geometry, which increases the need for high fabrication standards. As nanofabrication processes become increasingly standardized, incorporation of plasmonic nanostructures may also become industry standard for THz PCA technology.

## 5 Broadband Performance

### 5.1 Challenges

One of the attractive properties of pulsed THz emission from PCAs is the broadband nature of the emitted radiation. Typically, usable bandwidths in the range of 0.1 to 4 THz are readily achievable in LT-GaAs based PCA emitters pumped with 100-fs pulses.<sup>48</sup> There is significant motivation for increasing the spectral power density of higher frequency components. However, several challenges exist in standard THz TDS configurations that limit the usable frequency bandwidth. Broadband performance requires dipole antennas with uniform radiation resistance and low reactance across

**Table 3** Summary of plasmonic nanostructure enhanced THz PCAs.

	Advantages	Disadvantages	Key reported performance milestones
Gap located nanostructures	Increased quantum efficiency	Decreased gap dark resistivity and complex fabrication	2.1-nA peak THz current <sup>114</sup>
Nanostructured electrodes	Increased quantum efficiency and no increase in gap dark resistivity	Complex fabrication	3.8-mW output THz power, 5-THz bandwidth <sup>71</sup>

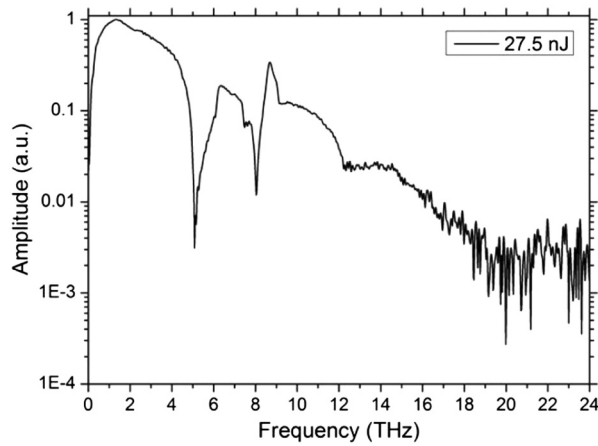


**Fig. 16** FFT amplitude as a function of frequency, showing a bandwidth approaching 20 THz. Reprinted from Ref. 135 with permission from OSA Publishing.

the desired bandwidth.<sup>140</sup> For the wide bandwidths desired in THz TDS, this often leads to a tradeoff with other performance characteristics.<sup>80</sup> There are also inherent limitations in the available bandwidth of the optical femtosecond pulse. Although narrower pulse widths with a wider available bandwidth are available, high THz frequency losses in the PCA substrate often prevent the extension bandwidths to higher frequencies using sub-100 fs excitation.<sup>75</sup> Propagation through the PCA substrate has a detrimental effect on the THz bandwidth, especially in GaAs. GaAs has a phonon absorption resonance centered at around 8.3 THz, as illustrated in the THz spectra shown in Fig. 16 [Fig. 2(b) in Ref. 135].<sup>135</sup> The absorption loss for a THz pulse propagating through 500  $\mu\text{m}$  (typical substrate thickness) of GaAs increases rapidly with frequency, falling to 50% of the original signal strength at around 3.3 THz.<sup>171</sup> This absorption loss is a major limiting factor in the bandwidth of the emitted THz pulses and is the reason that utilizing below 100-fs optical pulses in these configurations does not significantly improve the bandwidth.

## 5.2 Broadband Dipole Antenna

Early THz PCAs, as well as many still in use today, utilized simple dipole antenna structures such as parallel microstrip lines<sup>46</sup> or face-to-face dipoles<sup>45,78</sup> as the primary radiating elements. The major disadvantage of using such simple radiating elements is that they are inherently single and narrow band. Although the coherent detection nature of THz TDS systems offers high signal-to-noise,<sup>172</sup> losses outside of the dipole's resonant frequency range can be a significant source of performance degradation.<sup>80</sup> Utilizing established microwave engineering concepts, several works have aimed at implementing multi- and/or broadband dipole structures to improve the radiation efficiencies of these THz antennas.<sup>68,72,140,173–179</sup>

To the authors' best knowledge, the first attempt to study the use of broadband antennas in THz PCAs was made in 1991 by Dykaar et al.<sup>173</sup> This early work compared broadband log spiral and log periodic antenna patterns to simple face-to-face dipoles, with results indicating that the broadband antennas could yield an order of magnitude response improvement.<sup>173</sup> Log periodic antennas were also studied

by Gitin et al.<sup>174</sup> and Mendis et al.<sup>68</sup> In sub-0.1 THz frequencies, the response was found to be highly multiband, with resonant frequencies corresponding to the various lengths of the periodic elements.<sup>174</sup> Brown et al.<sup>175</sup> fabricated GaAs-based THz PCAs with square spiral antennas and tested their polarization characteristics in a photomixing configuration. This antenna was predicted to have a continuous, broadband response at lower THz frequencies (<1 THz). However, experimental results showed narrow resonance peaks occurring across the 0.1 to 1 THz measurement range. These results were attributed to the discrete nature of the antenna pattern, where each turn of the square spiral acted as an individual radiating element with a single, narrow resonance.<sup>175</sup> The same antenna was implemented in a pulsed optical excitation scheme to study the effects of photoconductive material and substrate.<sup>176,177</sup> A bullseye dipole with periodic grooves in the dipole metallization was studied by Liu et al.<sup>178</sup> This structure utilized THz frequency plasmon-polariton resonances along the periodic grooves to produce a narrow, two times greater resonance peak at a single frequency as compared to a simple dipole. Numerical simulations indicated that this resonance peak can be tuned by adjusting the size and period of the periodic grooves.<sup>178</sup> More recently, logarithmic spiral antennas were combined with nanostructured electrodes to improve the radiation efficiency of THz PCAs.<sup>72,140</sup> Numerical simulations indicated that the log spiral maintains a much more uniform radiation resistance and lower reactance than the more common bowtie dipoles, with experimental results showing around 4 $\times$  higher radiated powers.<sup>140</sup>

## 5.3 Ultrabroadband Emission and Detection

Standard configurations of THz TDS setups have a major inherent limitation of their usable bandwidth. In all TDS setups, the optical pulse excitation is incident on the electrode side of the PCA, since it would be unable to penetrate the optically thick substrate material to excite photocarriers in the dipole gap.<sup>43,48,78</sup> The generated THz radiation is emitted in both directions; however, the majority of TDS setups only utilize the forward propagating THz radiation (i.e., the radiation that passes through the PCA substrate, propagating in the same direction as the optical pulse). The reason for this is that it reduces the experimental setup complexity, since the optical and THz beam paths do not overlap.<sup>180</sup> Additionally, the majority of the radiated power propagate into the substrate, with the forward (in the substrate) to backward (in air) power ratio being dependent on the substrate permittivity ( $\epsilon_r$ ) on the order of  $\epsilon_r^{1/2}$  to  $\epsilon_r^{3/2}$ , depending on the antenna geometry.<sup>65</sup> As previously mentioned, this is at the cost of loss of bandwidth due to high frequency absorption in the GaAs substrate.

One of the first works observing this effect was reported by Kono et al.<sup>181</sup> Here, a SI InP electro-optic crystal pumped with 15-fs optical pulses was utilized as a source of broadband (>20 THz) radiation. The same 15-fs optical pump was utilized to gate a LT-GaAs PCA detector in a conventional setup, where the optical pump and THz beam are incident on opposite sides of the detector. A discontinuous frequency band up to around 20 THz was observed with a strong absorption band between 7 and 9 THz due to the GaAs detector substrate absorption.<sup>181</sup> Later works using a similar setup implemented a collinear detection scheme, where the optical

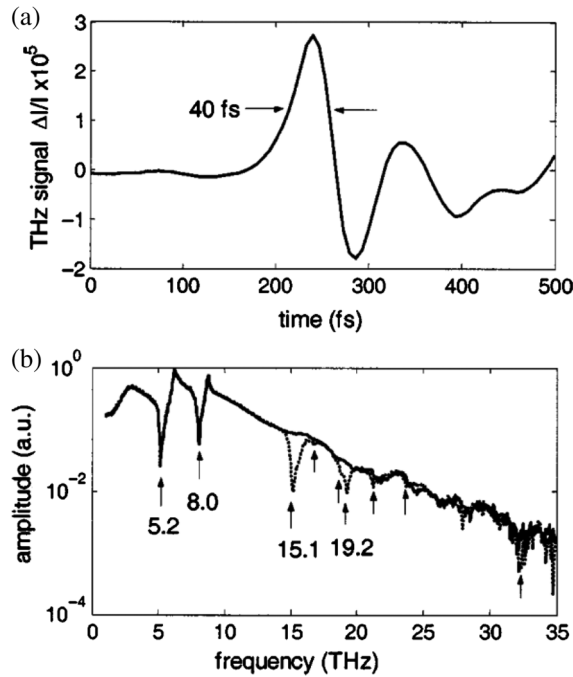


**Fig. 17** (a) The temporal THz wave form and (b) its corresponding Fourier transform amplitude spectrum (upper trace, solid line), together with spectrum measured in the presence of PTFE sample (lower trace, dotted line). Reprinted from Ref. 182, with permission of AIP Publishing.

gating pump of the detector was aligned with the transmitted THz radiation and both were incident on the antenna side of the detector.<sup>59,75,91,180</sup> PCAs gated with 15-fs pulses were demonstrated to achieve the same bandwidth as electro-optical sampling with a ZnTe crystal.<sup>75</sup> Modulation of the optical delay using the shaker method was utilized to measure time-derivatives of the THz waveforms, which expanded the detectable emission from a ZnTe crystal up to 60 THz.<sup>180</sup> Others have demonstrated the use of these broadband detection schemes to characterize vibrational modes in various materials, including cytidine<sup>182</sup> and maltose<sup>183</sup>. A 40-fs THz pulse measured by Shen et al.<sup>182</sup> is shown in Fig. 17(a) along with the Fourier transform spectrum illustrating a bandwidth beyond 30 THz in Fig. 17(b) (Fig. 2 in Ref. 182). Additionally, spectral measurements of polytetrafluoroethylene (PTFE) are shown as the dotted trace in Fig. 17(b). Here, PTFE vibrational modes up to 19.2 THz were observed.<sup>182</sup> More recent work has characterized the high power, broadband forward emission of a LT-GaAs PCA with interdigitated electrodes.<sup>135</sup> Here, a bandwidth of up to 20 THz was observed. Reducing the incident pulse power caused a uniform reduction of THz power across

the spectrum, while increasing the pulse width reduced the high frequency components of the signal.<sup>135</sup>

## 5.4 Summary and Outlooks

The advantages, disadvantages, and key performance milestones for plasmonic nanostructure THz PCAs are summarized in Table 4. The design of broadband antennas shows potential for increasing the useable THz bandwidth. However, it is clear that other factors such as varying polarization and resonant/no resonant regions across the desired operating band would likely need to be accounted for when implementing these complex antenna geometries into practical THz PCA systems. Shorter optical pulses and collection of surface emitted THz waves have demonstrated ultrabroadband pulse emission, reaching well into the far-infrared optical regime. However, since the optical beam cannot be isolated from the THz beam, safety becomes a concern for practical applications. Therefore, these configurations are currently limited to laboratory research.

## 6 Commercial Technologies

In addition to the various THz PCA emitters and systems described in the literature, several companies offer commercially available PCA-based THz systems, as well as individual PCA devices. Teraview Ltd., Picometrix LLC, Advantest, and Menlo Systems offer complete THz imaging and spectroscopy systems that utilize PCAs as their emitters and detectors. Teraview's TPS Spectra 3000 system utilizes LT-GaAs based PCAs, with 800-nm wavelength optical excitation.<sup>184</sup> Average optical power incident on the emitter is  $\sim 10$  mW, producing around  $1\text{-}\mu\text{W}$  average output THz power with up to 4-THz bandwidth (maximum frequency).<sup>184</sup> The newer TeraPulse 4000 system has a maximum 70-dB signal and  $\sim 80$ -dB SNR with bandwidth up to 6 THz.<sup>185</sup> Picometrix's T-Ray 5000 system utilizes LT-InGaAs PCAs for excitation at 1064-nm optical wavelength. The optical pump power is  $\sim 5$  mW, producing  $\sim 0.5\text{-}\mu\text{W}$  output THz pulse with an overall system SNR of  $>80$  dB and  $>4$  THz bandwidth.<sup>186</sup> Advantex's TAS series systems utilize PCAs under 1550-nm wavelength optical excitation to achieve up to 4 THz bandwidth and over 60-dB SNR.<sup>187</sup> Menlo Systems offers two THz spectroscopy systems: the TERA K8 and the TERA K15. The TERA K8 is based on  $\sim 800$ -nm optical excitation and offers over 3.5-THz bandwidth and over 70-dB SNR.<sup>188</sup> The TERA K15, on the other hand, claims to be the first commercial all fiber-coupled system utilizing 1560-nm optical excitation. This system has over 4-THz bandwidth, 75-dB SNR, and total dimensions comparable to a typical desktop computer.<sup>189</sup> The performance of the various systems is summarized in Table 5.

**Table 4** Summary of broadband performance of THz PCAs.

	Advantages	Disadvantages	Key reported performance milestones
Broadband dipole antenna design	Increased emission bandwidth	Trade-off with polarization control	4 $\times$ increased total THz power comparing log spiral to bowtie <sup>140</sup>
Ultrabroadband emission and detection	Full THz band coverage	Experimental setup not practical for many applications	60 THz detection bandwidth <sup>180</sup>

**Table 5** Summary of commercial PCA-based THz spectroscopy systems.

Company	Model	Bandwidth (max frequency)	SNR
Teraview	TPS Spectra 3000	4 THz	80 dB
Teraview	TeraPulse 4000	6 THz	80 dB
Picometrix	T-Ray 5000	4 THz	80 dB
Advantest	TAS	4 THz	60 dB
Menlo Systems	TERA K8	3.5 THz	70 dB
Menlo Systems	TERA K15	4 THz	75 dB

## 7 Concluding Remarks

From this review, it is apparent that there are many avenues to the ultimate goal of improving the performance of THz PCA technology. Each of these shows continuing promise for further improvement of THz TDS systems. However, it is likely that the next generation of pulsed THz systems will implement several of these methods to achieve superior performance as compared to current standard technology. This will allow the next generation of THz technology to exceed the current commercial systems that provide up to 6-THz bandwidth and 80-dB SNR.

## Acknowledgments

This work was supported in part by the National Science Foundation under Grant No. 1548550. This work was also supported through the University of Arkansas Engineering Research and Innovation Seed Funding Program and the University of Arkansas Doctoral Academy Fellowship.

## References

- C. Fattinger and D. Grischkowsky, "Terahertz beams," *Appl. Phys. Lett.* **54**, 490–492 (1989).
- L. A. Samoska, "An overview of solid-state integrated circuit amplifiers in the submillimeter-wave and THz regime," *IEEE Trans. Terahertz Sci. Technol.* **1**, 9–24 (2011).
- P. Dean et al., "Terahertz imaging using quantum cascade lasers—a review of systems and applications," *J. Phys. D: Appl. Phys.* **47**, 374008 (2014).
- A. Nahata, A. S. Weling, and T. F. Heinz, "A wideband coherent terahertz spectroscopy system using optical rectification and electro-optic sampling," *Appl. Phys. Lett.* **69**, 2321–2323 (1996).
- J. A. Fülöp et al., "Design of high-energy terahertz sources based on optical rectification," *Opt. Express* **18**, 12311–12327 (2010).
- M. D. King, W. D. Buchanan, and T. M. Korter, "Understanding the terahertz spectra of crystalline pharmaceuticals: terahertz spectroscopy and solid-state density functional theory study of (S)-(+)-ibuprofen and (RS)-ibuprofen," *J. Pharm. Sci.* **100**, 1116–1129 (2011).
- L. Ho, M. Pepper, and P. Taday, "Terahertz spectroscopy: signatures and fingerprints," *Nat. Photonics* **2**, 541–543 (2008).
- A. Grange, "Terahertz spectroscopy: an investigation into the use of terahertz radiation to detect/sense drugs, pharmaceuticals and polymorphs," Thesis, University of Leeds (2010).
- M. C. Kemp et al., "Security applications of terahertz technology," *Proc. SPIE* **5070**, 44 (2003).
- J. F. Federici et al., "THz imaging and sensing for security applications—explosives, weapons and drugs," *Semicond. Sci. Technol.* **20**, S266–S280 (2005).
- H.-B. Liu et al., "Terahertz spectroscopy and imaging for defense and security applications," *Proc. IEEE* **95**, 1514–1527 (2007).
- T. I. Jeon and D. Grischkowsky, "Characterization of optically dense, doped semiconductors by reflection THz time domain spectroscopy," *Appl. Phys. Lett.* **72**, 3032–3034 (1998).
- D. Hashimshony et al., "Characterization of the electrical properties and thickness of thin epitaxial semiconductor layers by THz reflection spectroscopy," *J. Appl. Phys.* **90**, 5778–5781 (2001).
- T. Kiwa et al., "Laser terahertz-emission microscope for inspecting electrical faults in integrated circuits," *Opt. Lett.* **28**, 2058–2060 (2003).
- N. Hasegawa et al., "Remote identification of protrusions and dents on surfaces by terahertz reflectometry with spatial beam filtering and out-of-focus detection," *Appl. Phys. Lett.* **83**, 3996–3998 (2003).
- M. Yamashita et al., "Noncontact inspection technique for electrical failures in semiconductor devices using a laser terahertz emission microscope," *Appl. Phys. Lett.* **93**, 2008–2010 (2008).
- I. Javaid, "Terahertz time of flight detection for absolute thickness," Thesis, University of North Carolina (2010).
- M. Yamashita et al., "THz emission characteristics from p/n junctions with metal lines under non-bias conditions for LSI failure analysis," *Opt. Express* **19**, 10864–10873 (2011).
- L. Minkevičius et al., "Detection of tab wire soldering defects on silicon solar cells using terahertz time-domain spectroscopy," *Electron. Lett.* **48**, 932 (2012).
- N. M. Burford et al., "Terahertz imaging for nondestructive evaluation of packaged power electronic devices," *Int. J. Emerg. Technol. Adv. Eng.* **4**, 395–401 (2014).
- F. Ospald et al., "Aeronautics composite material inspection with a terahertz time-domain spectroscopy system," *Opt. Eng.* **53**, 031208 (2013).
- P. C. Ashworth et al., "Terahertz pulsed spectroscopy of freshly excised human breast cancer," *Opt. Express* **17**, 12444–12454 (2009).
- A. M. Hassan et al., "Terahertz Imaging for margin assessment of breast cancer tumors," in *IEEE/MTT-S Int. Microwave Symp. Digest*, Vol. **12** (2012).
- C. Yu et al., "The potential of terahertz imaging for cancer diagnosis: a review of investigations to date," *Quant. Imaging Med. Surg.* **2**, 33–45 (2012).
- T. C. Bowman, M. El-shenawee, and L. K. Campbell, "Terahertz imaging of excised breast tumor tissue on paraffin sections," *IEEE Trans. Antennas Propag.* **63**, 2088–2097 (2015).
- T. C. Bowman, M. O. El-Shenawee, and L. C. Kampbell, "Terahertz transmission vs reflection imaging and model-based characterization for excised breast carcinomas," *Biomed. Opt. Express* **7**, 3756–3783 (2016).
- R. M. Woodward et al., "Terahertz pulse imaging in reflection geometry of human skin cancer and skin tissue," *Phys. Med. Biol.* **47**, 3853–3863 (2002).
- C. S. Joseph et al., "Imaging of ex vivo nonmelanoma skin cancers in the optical and terahertz spectral regions," *J. Biophotonics* **7**, 295–303 (2014).
- Z. D. Taylor et al., "Reflective terahertz imaging of porcine skin burns," *Opt. Lett.* **33**, 1258–1260 (2008).
- P. Tewari et al., "In vivo terahertz imaging of rat skin burns," *J. Biomed. Opt.* **17**, 040503 (2012).
- M. H. Arbab et al., "Terahertz spectroscopy for the assessment of burn injuries in vivo," *J. Biomed. Opt.* **18**, 077004 (2013).
- G. J. Wilmsink et al., "Development of a compact terahertz time-domain spectrometer for the measurement of the optical properties of biological tissues," *J. Biomed. Opt.* **16**, 047006 (2011).
- D. Crawley et al., "Three-dimensional terahertz pulse imaging of dental tissue," *J. Biomed. Opt.* **8**, 303–307 (2003).
- P. U. Jepsen, D. G. Cooke, and M. Koch, "Terahertz spectroscopy and imaging - modern techniques and applications," *Laser Photonics Rev.* **5**, 124–166 (2011).
- J. F. O'Hara, W. Withayachumnankul, and I. Al-Naib, "A review on thin-film sensing with terahertz waves," *J. Infrared Millimeter Terahertz Waves* **33**, 245–291 (2012).
- A. Redo-Sanchez et al., "Review of terahertz technology readiness assessment and applications," *J. Infrared Millimeter Terahertz Waves* **34**, 500–518 (2013).
- M. Haaser et al., "Terahertz pulsed imaging as an advanced characterisation tool for film coatings - a review," *Int. J. Pharm.* **457**, 510–520 (2013).
- S. K. Mathanker, P. R. Weckler, and N. Wang, "Terahertz (THz) applications in food and agriculture: a review," *Trans. ASABE* **56**, 1213–1226 (2013).
- A. Abina et al., "Applications of terahertz spectroscopy in the field of construction and building materials," *Appl. Spectrosc. Rev.* **50**, 279–303 (2014).
- X. Yang et al., "Biomedical applications of terahertz spectroscopy and imaging," *Trends Biotechnol.* **34**(10), 810–824 (2016).
- P. Shumyatsky and R. R. Alfano, "Terahertz sources," *J. Biomed. Opt.* **16**, 033001 (2011).
- D. H. Auston, "Subpicosecond electro-optic shock waves," *Appl. Phys. Lett.* **43**, 713–715 (1983).
- D. H. Auston, K. P. Cheung, and P. R. Smith, "Picosecond photoconducting Hertzian dipoles," *Appl. Phys. Lett.* **45**, 284–286 (1984).
- D. H. Auston et al., "Cherenkov radiation from femtosecond optical pulses in electro-optic media," *Phys. Rev. Lett.* **53**, 1555–1558 (1984).
- P. R. Smith, D. H. Auston, and M. C. Nuss, "Subpicosecond photoconducting dipole antennas," *IEEE J. Quantum Electron.* **24**, 255–260 (1988).

46. M. B. Ketchen et al., "Generation of subpicosecond electrical pulses on coplanar transmission-lines," *Appl. Phys. Lett.* **48**, 751–753 (1986).
47. C. Fattinger and D. Grischkowsky, "Point source terahertz optics," *Appl. Phys. Lett.* **53**, 1480–1482 (1988).
48. P. U. Jepsen, R. H. Jacobsen, and S. R. Keiding, "Generation and detection of terahertz pulses from biased semiconductor antennas," *J. Opt. Soc. Am. B* **13**, 2424 (1996).
49. H. Němec et al., "Carrier dynamics in low-temperature grown GaAs studied by terahertz emission spectroscopy," *J. Appl. Phys.* **90**, 1303–1306 (2001).
50. E. Moreno et al., "Time-domain numerical modeling of THz photoconductive antennas," *IEEE Trans. Terahertz Sci. Technol.* **4**, 490–500 (2014).
51. A. C. Warren et al., "Subpicosecond, freely propagating electromagnetic pulse generation and detection using GaAs:As epilayers," *Appl. Phys. Lett.* **58**, 1512–1514 (1991).
52. S. Gupta et al., "Subpicosecond carrier lifetime in GaAs grown by molecular beam epitaxy at low temperatures," *Appl. Phys. Lett.* **59**, 3276–3278 (1991).
53. E. S. Harmon et al., "Carrier lifetime versus anneal in low temperature growth GaAs," *Appl. Phys. Lett.* **63**, 2248–2250 (1993).
54. M. Tani et al., "Spectroscopic characterization of low-temperature grown GaAs epitaxial films," *Jpn. J. Appl. Phys.* **33**, 4807–4811 (1994).
55. M. Tani et al., "Emission characteristics of photoconductive antennas based on low-temperature-grown GaAs and semi-insulating GaAs," *Appl. Opt.* **36**, 7853–7859 (1997).
56. M. R. Stone et al., "Electrical and radiation characteristics of semilarge photoconductive terahertz emitters," *IEEE Trans. Microw. Theory Tech.* **52**, 2420–2429 (2004).
57. K. Moon et al., "Generation and detection of terahertz waves using low-temperature-grown GaAs with an annealing process," *ETRI J.* **36**, 159–162 (2014).
58. T. A. Liu, M. Tani, and C. L. Pan, "THz radiation emission properties of multienergy arsenic-ion-implanted GaAs and semi-insulating GaAs based photoconductive antennas," *J. Appl. Phys.* **93**, 2996–3001 (2003).
59. T. A. Liu et al., "Ultrabroadband terahertz field detection by photoconductive antennas based on multi-energy arsenic-ion-implanted GaAs and semi-insulating GaAs," *Appl. Phys. Lett.* **83**, 1322–1324 (2003).
60. B. Salem et al., "Pulsed photoconductive antenna terahertz sources made on ion-implanted GaAs substrates," *J. Phys. Condens. Matter* **17**, 7327–7333 (2005).
61. B. Salem et al., "Terahertz emission properties of arsenic and oxygen ion-implanted GaAs based photoconductive pulsed sources," *J. Vac. Sci. Technol.* **24**, 774–777 (2006).
62. B. Salem et al., "Improved characteristics of a terahertz set-up built with an emitter and a detector made on proton-bombarded GaAs photoconductive materials," *Semicond. Sci. Technol.* **21**, 283–286 (2006).
63. S. Winnerl et al., "Generation and detection of THz radiation with scalable antennas based on GaAs substrates with different carrier lifetimes," *IEEE J. Sel. Top. Quantum Electron.* **14**, 449–457 (2008).
64. M. Mikulics et al., "Photomixers fabricated on nitrogen-ion-implanted GaAs," *Appl. Phys. Lett.* **87**, 1–3 (2005).
65. D. Rutledge, D. Neikirk, and D. Kasilingam, *Infrared Millimeter Waves*, K. Button, Ed., pp. 1–90, Academic Press, Inc., New York (1983).
66. S. H. Yang et al., "Characterization of ErAs:GaAs and LuAs:GaAs superlattice structures for continuous-wave terahertz wave generation through plasmonic photomixing," *J. Infrared Millimeter Terahertz Waves* **37**, 640 (2016).
67. E. Budiarto et al., "High-intensity terahertz pulses at 1-kHz repetition rate," *IEEE J. Quantum Opt.* **32**, 1839–1846 (1996).
68. R. Mendis et al., "Tunable CW-THz system with a log-periodic photoconductive emitter," in *Proc. Int. Semicond. Device Res. Symp.*, Vol. **48**, pp. 318–319 (2003).
69. C. D. Wood et al., "Terahertz emission from metal-organic chemical vapor deposition grown Fe:InGaAs using 830 nm to 1.55  $\mu\text{m}$  excitation," *Appl. Phys. Lett.* **96**, 194104 (2010).
70. J. H. Kim, A. Polley, and S. E. Ralph, "Efficient photoconductive terahertz source using line excitation," *Opt. Lett.* **30**, 2490–2492 (2005).
71. N. T. Yardimci et al., "High-power terahertz generation using large-area plasmonic photoconductive emitters," *IEEE Trans. Terahertz Sci. Technol.* **5**, 223–229 (2015).
72. S. Yang et al., "7.5% optical-to-terahertz conversion efficiency offered by photoconductive emitters with three-dimensional plasmonic contact electrodes," *IEEE Trans. Terahertz Sci. Technol.* **4**, 575–581 (2014).
73. T. Hattori, K. Takamoto, and H. Nakatsuka, "Time-resolved study of intense terahertz pulses generated by a large-aperture photoconductive antenna," *Jpn. J. Appl. Phys.* **40**, 4907–4912 (2001).
74. B. Globisch et al., "Absolute terahertz power measurement of a time-domain spectroscopy system," *Opt. Lett.* **40**, 3544 (2015).
75. S. Kono, M. Tani, and K. Sakai, "Ultrabroadband photoconductive detection: comparison with free-space electro-optic sampling," *Appl. Phys. Lett.* **79**, 898–900 (2001).
76. C. W. Berry et al., "Significant performance enhancement in photoconductive terahertz optoelectronics by incorporating plasmonic contact electrodes," *Nat. Commun.* **4**, 1622 (2013).
77. P. K. Benicewicz, J. P. Roberts, and A. J. Taylor, "Scaling of terahertz radiation from large-aperture biased photoconductors," *J. Opt. Soc. Am. B* **11**, 2533–2546 (1994).
78. M. van Exter and D. R. Grischkowsky, "Characterization of an optoelectronic terahertz beam system," *IEEE Trans. Microw. Theory Tech.* **38**, 1684–1691 (1990).
79. J. T. Darrow et al., "Subpicosecond electromagnetic pulses from large-aperture photoconducting antennas," *Opt. Lett.* **15**, 323–325 (1990).
80. I. S. Gregory et al., "Optimization of photomixers and antennas for continuous-wave terahertz emission," *IEEE J. Quantum Electron.* **41**, 717–728 (2005).
81. K. Moon et al., "Nanoplasmonics enhanced terahertz sources," *Opt. Express* **22**, 27992–28001 (2014).
82. H. Tanoto et al., "Nano-antenna in a photoconductive photomixer for highly efficient continuous wave terahertz emission," *Sci. Rep.* **3**, 2824 (2013).
83. J. T. Darrow et al., "Saturation properties of large-aperture photoconducting antennas," *IEEE J. Quantum Electron.* **28**, 1607–1616 (1992).
84. E. R. Brown, "A photoconductive model for superior GaAs THz photomixers," *Appl. Phys. Lett.* **75**, 769–771 (1999).
85. S. E. Ralph and D. Grischkowsky, "Trap-enhanced fields in semi-insulators: the role of electrical and optical carrier injection," *Appl. Phys. Lett.* **59**, 1972–1974 (1991).
86. L. Hou and W. Shi, "An LT-GaAs terahertz photoconductive antenna with high emission power, low noise, and good stability," *IEEE Trans. Electron Devices* **60**, 1619–1624 (2013).
87. M. Suzuki and M. Tonouchi, "Fe-implanted InGaAs photoconductive terahertz detectors triggered by 1.56  $\mu\text{m}$  femtosecond optical pulses," *Appl. Phys. Lett.* **86**, 1–3 (2005).
88. S. Hadjiloucas, L. S. Karatzas, and J. W. Bowen, "Measurements of leaf water content using terahertz radiation," *IEEE Trans. Microw. Theory Tech.* **47**, 142–149 (1999).
89. C. Jordens et al., "Evaluation of leaf water status by means of permittivity at terahertz frequencies," *J. Biol. Phys.* **35**, 255–264 (2009).
90. D. H. Auston, "Picosecond optoelectronic switching and gating in silicon," *Appl. Phys. Lett.* **26**, 101–103 (1975).
91. T.-A. Liu et al., "Ultrabroadband terahertz field detection by proton-bombarded InP photoconductive antennas," *Opt. Express* **12**, 2954–2959 (2004).
92. L. Hou, W. Shi, and S. Chen, "Noise analysis and optimization of terahertz photoconductive emitters," *IEEE J. Sel. Top. Quantum Electron.* **19**, 8401305 (2013).
93. M. Suzuki and M. Tonouchi, "Fe-implanted InGaAs terahertz emitters for 1.56  $\mu\text{m}$  wavelength excitation," *Appl. Phys. Lett.* **86**, 1–3 (2005).
94. N. Chimot et al., "Terahertz radiation from heavy-ion-irradiated In<sub>0.53</sub>Ga<sub>0.47</sub>As photoconductive antenna excited at 1.55  $\mu\text{m}$ ," *Appl. Phys. Lett.* **87**, 193510 (2005).
95. A. Takazato et al., "Detection of terahertz waves using low-temperature-grown InGaAs with 1.56  $\mu\text{m}$  pulse excitation," *Appl. Phys. Lett.* **90**, 101119 (2007).
96. A. Takazato et al., "Terahertz wave emission and detection using photoconductive antennas made on low-temperature-grown InGaAs with 1.56  $\mu\text{m}$  pulse excitation," *Appl. Phys. Lett.* **91**, 011102 (2007).
97. O. Hatem et al., "Terahertz-frequency photoconductive detectors fabricated from metal-organic chemical vapor deposition-grown Fe-doped InGaAs," *Appl. Phys. Lett.* **98**, 121107 (2011).
98. R. Salas et al., "Growth and properties of rare-earth arsenide InGaAs nanocomposites for terahertz generation," *Appl. Phys. Lett.* **106**, 081103 (2015).
99. K. Murakumo et al., "Photoconductivity of Er-doped InAs quantum dots embedded in strain-relaxed InGaAs layers with 1.5  $\mu\text{m}$  cw and pulse excitation," *Jpn. J. Appl. Phys.* **55**, 04EH12 (2016).
100. M. Griebel et al., "Tunable subpicosecond optoelectronic transduction in superlattices of self-assembled ErAs nanoislands," *Nat. Mater.* **2**, 122–126 (2003).
101. A. Schwagmann et al., "Terahertz emission characteristics of ErAs: InGaAs-based photoconductive antennas excited at 1.55  $\mu\text{m}$ ," *Appl. Phys. Lett.* **96**, 141108 (2010).
102. H. Roehle et al., "Next generation 1.5 microm terahertz antennas: mesa-structuring of InGaAs/InAlAs photoconductive layers," *Opt. Express* **18**, 2296–2301 (2010).
103. R. J. B. Dietz et al., "THz generation at 1.55  $\mu\text{m}$  excitation: six-fold increase in THz conversion efficiency by separated photoconductive and trapping regions," *Opt. Express* **19**, 25911 (2011).
104. S. Preu et al., "1550 nm ErAs:In(Al)GaAs large area photoconductive emitters," *Appl. Phys. Lett.* **101**, 101105 (2012).
105. I. Kostakis, D. Saeedkia, and M. Missous, "Terahertz generation and detection using low temperature grown InGaAs-InAlAs photoconductive antennas at 1.55  $\mu\text{m}$  pulse excitation," *IEEE Trans. Terahertz Sci. Technol.* **2**, 617–622 (2012).
106. M. Mittendorff et al., "Large area photoconductive terahertz emitter for 1.55  $\mu\text{m}$  excitation based on an InGaAs heterostructure," *Nanotechnology* **24**, 214007 (2013).

107. R. J. B. Dietz et al., "64  $\mu\text{W}$  pulsed terahertz emission from growth optimized InGaAs/InAlAs heterostructures with separated photoconductive and trapping regions," *Appl. Phys. Lett.* **103**, 061103 (2013).
108. P. Gu et al., "Study of terahertz radiation from InAs and InSb," *J. Appl. Phys.* **91**, 5533–5537 (2002).
109. J. Sigmund et al., "Structure investigation of low-temperature-grown GaAsSb, a material for photoconductive terahertz antennas," *Appl. Phys. Lett.* **87**, 252103 (2005).
110. K. Bertulis et al., "GaBiAs: a material for optoelectronic terahertz devices," *Appl. Phys. Lett.* **88**, 201112 (2006).
111. C. M. Collier et al., "Photoconductive terahertz generation from textured semiconductor materials," *Sci. Rep.* **6**, 23185 (2016).
112. S. L. Chuang, *Physics of Photonic Devices*, p. 113, Wiley, Hoboken (2009).
113. M. Tani, K. Lee, and X.-C. Zhang, "Detection of terahertz radiation with low-temperature-grown GaAs-based photoconductive antenna using 1.55  $\mu\text{m}$  probe," *Appl. Phys. Lett.* **77**, 1396–1398 (2000).
114. A. Jooshesh et al., "Plasmon-enhanced below bandgap photoconductive terahertz generation and detection," *Nano Lett.* **15**, 8306–8310 (2015).
115. B. Sartorius et al., "All-fiber terahertz time-domain spectrometer operating at 1.5 micron telecom wavelengths," *Opt. Express* **16**, 9565–9570 (2008).
116. P. Juodawlkis and D. T. McInturf, "Ultrafast carrier dynamics and optical nonlinearities of low-temperature-grown InGaAs/InAlAs multiple quantum wells," *Appl. Phys. Lett.* **69**, 4062–4064 (1996).
117. R. J. B. Dietz et al., "Low temperature grown photoconductive antennas for pulsed 1060 nm excitation: Influence of excess energy on the electron relaxation," *J. Infrared Millimeter Terahertz Waves* **36**, 60–71 (2015).
118. R. J. B. Dietz et al., "Influence and adjustment of carrier lifetimes in InGaAs/InAlAs photoconductive pulsed terahertz detectors: 6 THz bandwidth and 90dB dynamic range," *Opt. Lett.* **22**, 615–623 (2014).
119. R. Ascáubi et al., "Enhanced terahertz emission from impurity compensated GaSb," *Phys. Rev. B* **72**, 1–5 (2005).
120. R. Ascáubi et al., "Terahertz emission from Ga1-xInxB," *Phys. Rev. B* **74**, 75323 (2006).
121. J. T. Darrow, X. C. Zhang, and D. H. Auston, "Power scaling of large-aperture photoconducting antennas," *Appl. Phys. Lett.* **58**, 25–27 (1991).
122. D. S. Kim and D. S. Citrin, "Coulomb and radiation screening in photoconductive terahertz sources," *Appl. Phys. Lett.* **88**, 86–89 (2006).
123. B. B. Hu et al., "Optically steerable photoconducting antennas," *Appl. Phys. Lett.* **56**, 886–888 (1990).
124. N. M. Froberg et al., "Terahertz radiation from a photoconducting antenna array," *IEEE J. Quantum Electron.* **28**, 2291–2301 (1992).
125. Y. Chen et al., "375-GHz-bandwidth photoconductive detector," *Appl. Phys. Lett.* **59**, 1984–1986 (1991).
126. S. Y. Chou, Y. Liu, and P. B. Fischer, "Terahertz GaAs metal-semiconductor-metal photodetectors with nanoscale finger spacing and width," *Appl. Phys. Lett.* **61**, 477–479 (1992).
127. E. R. Brown et al., "Milliwatt output levels and superquadratic bias dependence in a low-temperature-grown GaAs photomixer," *Appl. Phys. Lett.* **64**, 3311–3313 (1994).
128. E. R. Brown et al., "Photomixing up to 3.8 THz in low-temperature-grown GaAs," *Appl. Phys. Lett.* **66**, 285–287 (1995).
129. A. Dreyhaupt et al., "High-intensity terahertz radiation from a microstructured large-area photoconductor," *Appl. Phys. Lett.* **86**, 121114 (2005).
130. T. Hattori et al., "Intense terahertz pulses from large-aperture antenna with interdigitated electrodes," *Jpn. J. Appl. Phys.* **45**, L422–L424 (2006).
131. M. Awad et al., "Characterization of low temperature GaAs antenna array terahertz emitters," *Appl. Phys. Lett.* **91**, 181124 (2007).
132. F. Peter et al., "Coherent terahertz detection with a large-area photoconductive antenna," *Appl. Phys. Lett.* **91**, 1–4 (2007).
133. G. Acuna et al., "Interdigitated terahertz emitters," *Electron. Lett.* **44**, 229–231 (2008).
134. J. Madéo et al., "Frequency tunable terahertz interdigitated photoconductive antennas," *Electron. Lett.* **46**, 611 (2010).
135. P. J. Hale et al., "20 THz broadband generation using semi-insulating GaAs interdigitated photoconductive antennas," *Opt. Express* **22**, 26358–26364 (2014).
136. M. Beck et al., "Impulsive terahertz radiation with high electric fields from an amplifier-driven large-area photoconductive antenna," *Opt. Express* **18**, 9251–9257 (2010).
137. S. Winnerl, "Scalable microstructured photoconductive terahertz emitters," *J. Infrared Millimeter Terahertz Waves* **33**, 431–454 (2012).
138. G. Klatt et al., "Terahertz emission from lateral photo-Dember currents," *Opt. Express* **18**, 4939–4947 (2010).
139. G. Klatt et al., "Large-area laser-driven terahertz emitters," *Electron. Lett.* **46**, S24–S26 (2010).
140. C. W. Berry, M. R. Hashemi, and M. Jarrahi, "Generation of high power pulsed terahertz radiation using a plasmonic photoconductive emitter array with logarithmic spiral antennas," *Appl. Phys. Lett.* **104**, 081122 (2014).
141. A. Singh and S. S. Prabhu, "Microlensless interdigitated photoconductive terahertz emitters," *Opt. Express* **23**, 1529 (2015).
142. B. Lee et al., "Review on subwavelength confinement of light with plasmonics," *J. Mod. Opt.* **57**, 1479–1497 (2010).
143. Y. A. Akimov and W. S. Koh, "Design of plasmonic nanoparticles for efficient subwavelength light trapping in thin-film solar cells," *Plasmonics* **6**, 155–161 (2011).
144. N. Burford and M. El-Shenawee, "Plasmonic enhancement of irregular shape nano-patch for thin film silicon solar cells," *Appl. Comput. Electromagn. Soc. J.* **28**, 359–373 (2013).
145. N. Burford and M. El-Shenawee, "Optimization of silver nanotoroid arrays for the absorption enhancement of silicon thin-film solar cells," *Plasmonics* **10**, 225–232 (2014).
146. K. R. Catchpole and A. Polman, "Plasmonic solar cells," *Opt. Express* **16**, 21793–800 (2008).
147. H. A. Atwater and A. Polman, "Plasmonics for improved photovoltaic devices," *Nat. Mater.* **9**, 205–213 (2010).
148. X. C. Zhang et al., "Terahertz optical rectification from a nonlinear organic crystal," *Appl. Phys. Lett.* **61**, 3080–3082 (1992).
149. S. Varma et al., "Plasma enhancement of femtosecond laser-induced electromagnetic pulses at metal and dielectric surfaces," *Opt. Eng.* **53**, 051515 (2014).
150. R. N. Singh et al., "Properties of nonlinear optical crystals in the terahertz wavelength region," *Opt. Eng.* **45**, 094002 (2006).
151. G. Welsh and N. Hunt, "Terahertz emission from nano-structured metal surfaces," in *15th Int. Conf. on Ultrafast Phenomena*, pp. 1–3 (2006).
152. G. H. Welsh, N. T. Hunt, and K. Wynne, "Terahertz-pulse emission through laser excitation of surface plasmons in a metal grating," *Phys. Rev. Lett.* **98**, 3–6 (2007).
153. G. H. Welsh and K. Wynne, "Generation of ultrafast terahertz radiation pulses on metallic nanostructured surfaces," *Opt. Express* **17**, 2470–2480 (2009).
154. Y. Gao et al., "Analysis of terahertz generation via nanostructure enhanced plasmonic excitations," *J. Appl. Phys.* **106**, 074302 (2009).
155. D. K. Polyushkin et al., "THz generation from plasmonic nanoparticle arrays," *Nano Lett.* **11**, 4718–4724 (2011).
156. G. Ramakrishnan et al., "Plasmon-enhanced terahertz emission from a semiconductor/metal interface," *Appl. Phys. Lett.* **104**, 071104 (2014).
157. G. K. P. Ramanandan, A. J. L. Adam, and P. C. M. Planken, "Enhanced terahertz emission from schottky junctions using plasmonic nanostructures," *ACS Photonics* **1**, 1165–1172 (2014).
158. S. Park et al., "Nanoplasmonic photoconductive antenna for high power terahertz emission," in *16th Int. Solid-State Sensors, Actuators and Microsystems Conf.*, pp. 2498–2501 (2011).
159. S.-G. Park et al., "Terahertz photoconductive antenna with metal nanoislands," *Opt. Express* **20**, 25530 (2012).
160. S. G. Park et al., "Enhancement of terahertz pulse emission by optical nanoantenna," *ACS Nano* **6**, 2026–2031 (2012).
161. A. Jooshesh et al., "Nanoplasmonics enhanced terahertz sources," *Opt. Express* **22**, 27992–28001 (2014).
162. O. Mitrofanov et al., "Photoconductive terahertz near-field detector with a hybrid nanoantenna array cavity," *ACS Photonics* **2**, 1763–1768 (2015).
163. S. Zhong et al., "FDTD study of a novel terahertz emitter with electrical field enhancement using surface plasmon resonance," *PIERS Online* **6**, 153–156 (2010).
164. C. W. Berry and M. Jarrahi, "Terahertz generation using plasmonic photoconductive gratings," *New J. Phys.* **14**, 105029 (2012).
165. B. Y. Hsieh and M. Jarrahi, "Analysis of periodic metallic nanoslits for efficient interaction of terahertz and optical waves at nanoscale dimensions," *J. Appl. Phys.* **109**, 084326 (2011).
166. S. Yang et al., "Compact terahertz radiation source using a bimodal laser and plasmonic photomixer," *SPIE Newsroom* **1**, 2–4 (2016).
167. K. Moon et al., "Bias field tailored plasmonic nano-electrode for high-power terahertz photonic devices," *Sci. Rep.* **5**, 13817 (2015).
168. B. Heshmat et al., "Nanoplasmonic terahertz photoconductive switch on GaAs," *Nano Lett.* **12**, 6255–6259 (2012).
169. S. C. Corzo-Garcia, M. Alfaro, and E. Castro-Camus, "Transit time enhanced bandwidth in nanostructured terahertz emitters," *J. Infrared Millimeter Terahertz Waves* **35**(12), 987–992 (2014).
170. N. B. Burford and M. O. El-Shenawee, "Computational modeling of plasmonic thin-film terahertz photoconductive antennas," *J. Opt. Soc. Am. B* **33**, 748–759 (2016).
171. C. T. A. Johnk, *Engineering Electromagnetic Fields and Waves*, Wiley, Hoboken (1988).
172. S. Mickan et al., "Analysis of system trade-offs for terahertz imaging," *Microelectron. J.* **31**, 503–514 (2000).
173. D. R. Dykaar et al., "Log-periodic antennas for pulsed terahertz radiation," *Appl. Phys. Lett.* **59**, 262–264 (1991).
174. M. M. Gitin et al., "Broadband characterization of millimeter-wave log-periodic antennas by photoconductive sampling," *IEEE Trans. Antennas Propag.* **42**, 335–339 (1994).

175. E. R. Brown et al., "Characterization of a planar self-complementary square-spiral antenna in the THz region," *Microw. Opt. Technol. Lett.* **48**, 524–529 (2006).
176. Z. D. Taylor et al., "Resonant-optical-cavity photoconductive switch with 0.5% conversion efficiency and 1.0 W peak power," *Opt. Lett.* **31**, 1729–1731 (2006).
177. J. Y. Suen et al., "Characterization and modeling of a terahertz photoconductive switch," *Appl. Phys. Lett.* **96**, 141103 (2010).
178. S. Liu, X. Shou, and A. Nahata, "Coherent detection of multiband terahertz radiation using a surface plasmon-polariton based photoconductive antenna," *IEEE Trans. Terahertz Sci. Technol.* **1**, 412–415 (2011).
179. H. Ito et al., "Broadband photonic terahertz-wave emitter integrating untraveling-carrier photodiode and self-complementary planar antenna," *Opt. Eng.* **53**, 031209 (2014).
180. S. Kono, M. Tani, and K. Sakai, "Coherent detection of mid-infrared radiation up to 60 THz with an LT-GaAs photoconductive antenna," *Optoelectron. IEE* **149**, 105–109 (2002).
181. S. Kono et al., "Detection of up to 20 THz with a low-temperature-grown GaAs photoconductive antenna gated with 15 fs light pulses," *Appl. Phys. Lett.* **77**, 105–109 (2000).
182. Y. C. Shen et al., "Ultrabroadband terahertz radiation from low-temperature-grown GaAs photoconductive emitters," *Appl. Phys. Lett.* **83**, 3117–3119 (2003).
183. Y. C. Shen et al., "Generation and detection of ultrabroadband terahertz radiation using photoconductive emitters and receivers," *Appl. Phys. Lett.* **85**, 164–166 (2004).
184. *TPS Spectra 3000*, Teraview LTD, Cambridge, United Kingdom.
185. *TeraPulse 4000*, Teraview LTD, Cambridge, United Kingdom.
186. *T-Ray 3000*, Picometrix, Ann Arbor.
187. *TAS7500*, Advantest, Tokyo, Japan.
188. *TERA K8*, MenloSystems, Martinsried, Germany.
189. *TERA K15*, MenloSystems, Martinsried, Germany.

**Nathan M. Burford** received his BSc degree in physics from Southeast Missouri State University in 2011 and his MSc and PhD degrees in microelectronics-photonics from the University of Arkansas in 2013 and 2017, respectively. He is an NSF GK-12, NSF I-Corps, and University of Arkansas Doctoral Academy Fellow. His research interests include computational design for plasmonic optoelectronic devices, nanofabrication processes, electromagnetic metamaterials, and THz imaging and spectroscopy, and he currently works for WattGlass in Fayetteville, Arkansas.

**Magda O. El-Shenawee** received her PhD in electrical engineering from the University of Nebraska, Lincoln, in 1991. Her research interests include terahertz imaging and spectroscopy, photoconductive antennas, microwave and millimeter wave characterization of materials, computational electromagnetics, inverse scattering algorithms, MEMS antennas, nanoplasmonic antennas, and biopotentials modeling of breast tumors. She published over 200 journal and conference papers coauthored with her graduate students and postdoctoral fellow, and two book chapters coauthored with colleagues from other universities.